TOWARDS NONLINEAR DISENTANGLEMENT IN NATURAL DATA WITH TEMPORAL SPARSE CODING

Anonymous authors
Paper under double-blind review

ABSTRACT

Disentangling the underlying generative factors from complex data has so far been limited to carefully constructed scenarios. We propose a path towards evaluation on natural data by first showing that the statistics of natural data provide enough structure to enable disentanglement, both theoretically and empirically. Specifically, we provide evidence that objects in natural movies undergo transitions that are typically small in magnitude with occasional large jumps, which is characteristic of a temporally sparse distribution. To address this finding we provide a novel proof that relies on a sparse prior on temporally adjacent observations to recover the true latent variables up to permutations and sign flips, directly providing a stronger result than previous work. We show that equipping practical estimation methods with our prior often surpasses the current state-of-the-art on several established benchmark datasets without any impractical assumptions, such as knowledge of the number of changing generative factors. Furthermore, we contribute two new benchmarks, Natural Sprites and KITTI Masks, which integrate the measured natural dynamics to enable disentanglement evaluation with more realistic datasets. We leverage these benchmarks to test our theory, demonstrating improved performance. We also identify non-obvious challenges for current methods in scaling to more natural domains. Taken together our work addresses key issues in disentanglement research for moving towards more natural settings.

1 INTRODUCTION

Natural scene understanding can be achieved by decomposing the signal into its underlying factors of variation. An intuitive approach for this problem (Bengio et al., 2013) assumes that a visual representation of the world can be constructed via a generative process that receives factors as input and produces natural signals as output. Although untrue in the literal sense, this point of view is justified by the fact that our world is composed of distinct entities that can vary independently, but with regularity imposed by physics. A desired solution to this problem is to avoid *non-identifiability*, which means a set of possible solutions may all appear equally valid to the model, while only one identifies the true generative factors.

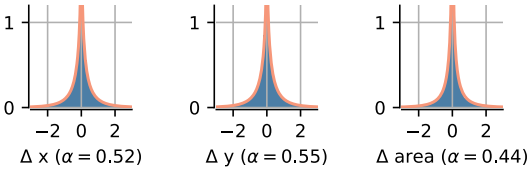

Figure 1: **Statistics of Natural Transitions**. The histograms show distributions over transitions of segmented object masks from natural videos for horizontal and vertical position as well as object size. The red lines indicate fits of generalized Laplace distributions (2) with shape value α. Data shown is for object masks extracted from YouTube videos. See Appendix H for similar measurements from the KITTI self-driving car dataset.

Our work is motivated by the question of whether identifiability can be achieved using assumptions that are predicated on natural data. Our core observation that enables us to make progress in addressing this question is that *natural data have sparse transitions*. To estimate the generative factors of natural data, we compute statistics on measured transitions of area and position for object masks from large-scale, natural, unstructured videos. Specifically, we extracted over 300,000 object segmentation mask transitions from YouTube-VOS (Xu et al., 2018; Yang et al., 2019) and KITTI-MOTS (Voigtlaender et al., 2019; Geiger et al., 2012; Milan et al., 2016) (discussed in detail in Appendix H). We fit generalized Laplace distributions to the collected data (equation (2)), which we indicate with red lines

in Fig. 1. We see empirically that all distributions of temporal transitions are highly sparse. With this information at hand, we are able to provide a proof for capturing the underlying generative factors of the data up to permutations and sign flips in the case of sparse transitions that is not covered by previous work (Hyvärinen and Morioka, 2016).

In total, our contributions are: With measurements from unstructured natural video annotations we provide evidence that natural generative factors undergo sparse changes across time. We provide a proof of identifiability that relies on the observed sparse innovations to identify nonlinearly mixed sources up to a permutation and sign-flip, which we then validate with practical estimation methods for empirical comparisons. We leverage the natural scene information to create novel datasets where the latent transitions between frames follow natural statistics, providing a benchmark to evaluate the practical capabilities of models in uncovering the true latent generative factors in the presence of realistic dynamics. We demonstrate improved disentanglement over previous models on existing datasets and our contributed ones with quantitative metrics from both the disentanglement (Locatello et al., 2018) and the nonlinear ICA community (Hyvärinen and Morioka, 2016). We show via numerous visualization techniques that the learned representations for competing models have important differences, even when quantitative metrics suggest that they are performing equally well.

2 Related Work – Disentanglement and Nonlinear ICA

Disentangled representation learning has its roots in blind source separation (Jutten and Herault, 1991) and shares goals fields such as inverse graphics (Kulkarni et al., 2015; Yildirim et al., 2020) and developing models of invariant neural computation (Wiskott and Sejnowski, 2002; Hyvärinen and Hoyer, 2000)(see Bengio et al., 2013, for a review). A disentangled representation would be valuable for a wide variety of machine learning applications, including sample efficiency for downstream tasks (Locatello et al., 2018; Gao et al., 2019), fairness (Locatello et al., 2019; Creager et al., 2019) and interpretability (Bengio et al., 2013; Higgins et al., 2017; Adel et al., 2018). Since there is no agreed upon definition of disentanglement in the literature, we adopt two common measurable criteria: i) each encoding element represents a single generative factor and ii) the values of generative factors are trivially decodable from the encoding (Ridgeway and Mozer, 2018; Eastwood and Williams, 2018).

Uncovering the underlying factors of variation has been a long-standing goal in independent component analysis (ICA) (Jutten and Herault, 1991; Bell and Sejnowski, 1995; Hyvärinen and Pajunen, 1999; Barron and Malik, 2012; Sohl-Dickstein et al., 2010). ICA (Comon, 1994) provides an identifiable solution for disentangling data mixed via linear generators receiving non-Gaussian factors as input. Recently, unsupervised approaches towards this goal have largely been based on Variational Autoencoders (VAEs) (Kingma and Welling, 2013) and have assumed that the data is independent and identically distributed (*i.i.d.*) (Locatello et al., 2018) even though nonlinear methods that make this *i.i.d.* assumption have been proven to be *non-identifiable* (Hyvärinen and Pajunen, 1999; Locatello et al., 2018). Nonetheless, the bottom-up approach of starting with a nonlinear generator that produces well-controlled data has led to considerable achievements in understanding nonlinear disentanglement in VAEs (Higgins et al., 2017; Burgess et al., 2018; Rolinek et al., 2019; Chen et al., 2018), consolidating ideas from neural computation and machine learning (Khemakhem et al., 2020), and seeking a principled definition of disentanglement (Higgins et al., 2018; Ridgeway, 2016; Eastwood and Williams, 2018; Hyvärinen and Pajunen, 1999).

Recently, Hyvärinen and colleagues (Hyvärinen and Morioka, 2016; 2017; Hyvärinen et al., 2018; Khemakhem et al., 2020) showed that a solution to the non-identifiability of nonlinear ICA can be found by assuming that generative factors are conditioned on an additional observed variable, such as past states or the time index itself. This contribution was generalized by Khemakhem et al. (2020) past the nonlinear ICA domain to any consistent parameter estimation method for deep latent-variable models, including the VAE framework. However, the theoretical assumptions underlying this branch of work do not account for the sparse transitions we observe in the statistics of natural scenes, which we discuss in further detail in appendix G. Another branch of work requires some form of supervision (Szabó et al., 2017; Shu et al., 2019; Locatello et al., 2020), namely regarding the number of factors changed. Locatello et al. (2020) proposed an approach to estimate this required knowledge at runtime, however their assumptions underlying identifiability may not be satisfied in practice. The motivation

of our method and dataset contributions is to address these limitations and to enable unsupervised disentanglement learning in more naturalistic scenarios[1].

The fact that physical processes bind generative factors in temporally adjacent natural video segments has been thoroughly explored for learning in neural networks (Hinton, 1990; Földiák, 1991; Mitchison, 1991; Wiskott and Sejnowski, 2002; Hyvärinen et al., 2003; Denton and Birodkar, 2017). We propose a method that uses time information in the form of an L_1-*sparse* temporal prior, which is motivated by the natural scene measurements presented above as well as by previous work (Simoncelli and Olshausen, 2001; Olshausen, 2003; Hyvärinen et al., 2003; Cadieu and Olshausen, 2012). Such a prior would intuitively allow for sharp changes in some latent factors, while most other factors remain unchanged between adjacent time-points. Almost all similar methods are variants of slow feature analysis (SFA, Wiskott and Sejnowski, 2002), which measure slowness in terms of the Euclidean (i.e. L_2, or log Gaussian) distance between temporally adjacent encodings. Related to our approach, a probabilistic interpretation of SFA has been previously proposed (Turner and Sahani, 2007), as well as extensions to variational inference (Grathwohl and Wilson, 2016). Additionally, Hashimoto (2003) suggested that a sparse (Cauchy) slowness prior improves correspondence to biological complex cells over the L_2 slowness prior in a two-layer model. However, to the best of our knowledge an L_1 temporal prior has previously only been used in deep auto-encoder frameworks when applied to semi-supervised tasks (Mobahi et al., 2009; Zou et al., 2012), and was mentioned in (Cadieu and Olshausen, 2012), which used an L_2 prior, but claimed that an L_1 prior performed similarly on their task. Inspired by Hyvärinen et al. (Hyvärinen and Morioka, 2016; Hyvärinen et al., 2018), we only assume that the latent factors are temporally dependent, thus avoiding assuming knowledge of the number of factors where the two observations differ (Shu et al., 2019), which Locatello et al. (2020) estimate during evaluation.

Most of the standard datasets for disentanglement (dSprites (Matthey et al., 2017), Cars3D (Reed et al., 2015), SmallNORB (LeCun et al., 2004), Shapes3D (Kim and Mnih, 2018), MPI3D (Gondal et al., 2019)) have been compiled into a disentanglement library (DisLib) by Locatello et al. (2018). However, all of the DisLib datasets are limited in that the data generating process is independent and identically distributed (*i.i.d.*) and all generative factors are assumed to be discrete. In a follow-up study, Locatello et al. (2020) proposed combining pairs of images such that only k factors change, as this matches their modeling assumptions required to prove identifiability, where $k \in \mathcal{U}\{1, D-1\}$ and D denotes the number of ground-truth factors, which are then sampled uniformly. We additionally use the measurements from Fig. 1 to construct datasets which can be used for evaluating disentanglement, but where the change in pairs of images directly corresponds to natural dynamics.

3 Theory

3.1 Generative Model

We have provided evidence to support the hypothesis that generative factors of natural videos have sparse temporal transitions (see Fig. 1). To mimic this process, we assume temporally adjacent input pairs $(\mathbf{x}_{t-1}, \mathbf{x}_t)$ coming from a nonlinear generator that maps factors to images $\mathbf{x} = g(\mathbf{z})$, where pairs of generative factors form a Markov chain:

$$p(\mathbf{z}_t, \mathbf{z}_{t-1}) = p(\mathbf{z}_t|\mathbf{z}_{t-1})p(\mathbf{z}_{t-1}). \tag{1}$$

Assume the observed data $(\mathbf{x}_t, \mathbf{x}_{t-1})$ comes from the following generative process:

$$\mathbf{x} = g(\mathbf{z}), \quad p(\mathbf{z}_{t-1}) = \prod_{i=1}^{d} p(z_{t-1,i}), \quad p(\mathbf{z}_t|\mathbf{z}_{t-1}) = \prod_{i=1}^{d} \frac{\alpha\lambda}{2\Gamma(1/\alpha)} \exp -(\lambda|z_{t,i} - z_{t-1,i}|^{\alpha}), \tag{2}$$

where λ is the distribution rate, $p(\mathbf{z}_{t-1})$ is a factorized Gaussian prior $\mathcal{N}(\mathbf{0}, \mathbf{I})$ (as in Kingma and Welling, 2013) and $p(\mathbf{z}_t|\mathbf{z}_{t-1})$ is a factorized generalized Laplace distribution (Bethge, 2006; Sinz et al., 2009) with shape parameter α, which determines the shape and especially the kurtosis of the function[2]. Intuitively, smaller α implies larger kurtosis and sparser temporal transitions of the

[1] As in slow feature analysis, we consider learning from videos without labels as *unsupervised*.

[2] For a stationary stochastic process, $p(\mathbf{z}_{t-1})$ represents the instantaneous marginal distribution and $p(\mathbf{z}_t|\mathbf{z}_{t-1})$ the transition distribution. In case of an autoregressive process with non-Gaussian innovations with finite variance, it follows from the central limit theorem that the marginal distribution converges to a Gaussian in the limit of large λ.

generative factors (special cases are Gaussian, $\alpha = 2$, and Laplacian, $\alpha = 1$). Critically, for our proof we assume $\alpha < 2$ to ensure that temporal transitions are sparse. Like Locatello et al. (2020), we assume that noise is modeled indirectly as a latent variable and is manifested through the generator g.

The novelty of our approach lies in our explicit modeling of sparse transitions, which results in a stronger identifiability proof than previously achieved, a scalable implementation, and assurance that we cover the transition statistics of natural data (Hyvärinen and Morioka, 2017; Khemakhem et al., 2020) (see Appendix G for a more detailed comparison).

3.2 Identifiability Proof

Theorem 1 *For a ground-truth $(g^*, \lambda^*, \alpha^*)$ and a learned (g, λ, α) model as defined in equation (2), if the functions g^* and g are injective and differentiable almost everywhere, $\lambda^* = \lambda$, $\alpha^* = \alpha < 2$ (i.e. there is no model misspecification) and the distributions of pairs of images generated from the priors $\mathbf{z}^* \sim p^*(\mathbf{z})$ and $\mathbf{z} \sim p(\mathbf{z})$ are matched $(g^*(\mathbf{z}^*_{t-1}), g^*(\mathbf{z}^*_t)) = (g(\mathbf{z}_{t-1}), g(\mathbf{z}_t))$ almost everywhere, then $g = g^* \circ \sigma$, where σ is a permutation with sign flipping.*

The formal proof is provided in Appendix B.1. It implies that if the temporal changes of ground-truth factors are sparse, then the only generator consistent with the observations is the ground-truth one (up to a permutation and sign flips). The main idea behind the proof is to represent g as $g^* \circ h$ and note that if h were not a permutation, then the distributions $((g^* \circ h)(\mathbf{z}_{t-1}), (g^* \circ h)(\mathbf{z}_t))$ and $(g^*(\mathbf{z}^*_{t-1}), g^*(\mathbf{z}^*_t))$ would not match, due to the injectivity of g^*.

Fig. 2 illustrates why the model defined in equation (2) has a unique generator. The crucial point is that we consider pairs of images, which differ effectively in only a few factors of variation due to the sparse prior ($\alpha < 2$). The 2D latent representations of such pairs are shown as blue points connected by lines. If the function h were not a permutation, it would map these latent points into a configuration in which many of the connecting lines are not parallel to one of the axes. However, the ground-truth generator, g^*, should still map this transformed latent space to the observed pairs of images differing in a few factors of variation, which contradicts it being injective. Moreover, Fig. 2 also illustrates that a rotationally symmetric Gaussian prior ($\alpha = 2$) on the transitions in either the generative or the learned model would make the problem non-identifiable. Similar to linear ICA, but in the temporal domain, we therefore have to assume that the transitions of generative factors across time be non-Gaussian.

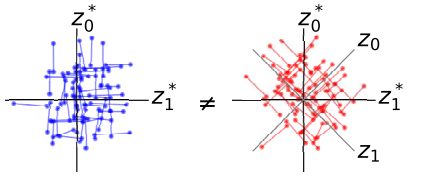

$\Rightarrow (g^*(z^*_{t-1}), g^*(z^*_t)) \neq (g(z_{t-1}), g(z_t))$

Figure 2: **Proof illustration**. Connected points indicate pairs of samples for the generative model (left) and for an entangled learned model (right). The relation means inequality in distribution.

3.3 Slow Variational Autoencoder

In order to validate our proof, we must choose a probabilistic latent variable model for estimating the data density. We chose to build upon the framework of VAEs because of their efficiency in estimating a variational approximation to the ground truth posterior of a deep latent variable model (Kingma and Welling, 2013). In Appendix C we also note their shortcomings and discuss alternative approaches.

The standard VAE objective assumes *i.i.d.* data and a standard normal prior with diagonal covariance on the learned latent representations $\mathbf{z} \sim \mathcal{N}(\mathbf{0}, \mathbf{I})$. To extend this to sequences, we assume the same functional form for our model prior as in equation (1) and (2). The posterior of our model is independent across time steps. Specifically,

$$q(\mathbf{z}_t, \mathbf{z}_{t-1}|\mathbf{x}_t, \mathbf{x}_{t-1}) = q(\mathbf{z}_t|\mathbf{x}_t)\, q(\mathbf{z}_{t-1}|\mathbf{x}_{t-1}), \quad q(\mathbf{z}|\mathbf{x}) = \prod_{i=1}^{d} \mathcal{N}(\mu_i(\mathbf{x}), \sigma_i^2(\mathbf{x})), \tag{3}$$

where $\mu_i(\mathbf{x})$ and $\sigma_i^2(\mathbf{x})$ are the input-dependent mean and variance of our model's posterior. We visualize this combination of priors and posteriors in Fig. 3. For a given pair of inputs $(\mathbf{x}_t, \mathbf{x}_{t-1})$, the full ELBO (which we derive in B.2) can be written as

$$\begin{aligned}\mathcal{L}(\mathbf{x}_t, \mathbf{x}_{t-1}) = {} & E_{q(\mathbf{z}_t, \mathbf{z}_{t-1}|\mathbf{x}_t, \mathbf{x}_{t-1})}[\log p(\mathbf{x}_t, \mathbf{x}_{t-1}|\mathbf{z}_t, \mathbf{z}_{t-1})] - D_{KL}(q(\mathbf{z}_{t-1}|\mathbf{x}_{t-1})|p(\mathbf{z}_{t-1})) \\ & - \gamma\, E_{q(\mathbf{z}_{t-1}|\mathbf{x}_{t-1})}[D_{KL}(q(\mathbf{z}_t|\mathbf{x}_t)|p(\mathbf{z}_t|\mathbf{z}_{t-1}))],\end{aligned} \tag{4}$$

where γ is a regularization term for the sparsity prior, analogous to β in β-VAEs (Higgins et al., 2017). The first term on the right-hand side is the log-likelihood (i.e. the negative reconstruction error, with $p(\mathbf{x}_t, \mathbf{x}_{t-1}|\mathbf{z}_t, \mathbf{z}_{t-1})$ parameterized by the decoder of the VAE), the second term is the KL to a normal prior as in the standard VAE and the last term is an expectation of the KL between the posterior at time step t and the conditional prior $p(\mathbf{z}_t|\mathbf{z}_{t-1})$. The expectation in the last term is taken over samples from the posterior at the previous time step $q(\mathbf{z}_{t-1}|\mathbf{x}_{t-1})$. We observe that taking the mean $\mu(\mathbf{x}_{t-1})$ as a single sample is sufficient (analogous to the log-likelihood that is typically evaluated at a single sample from the posterior).

In practice, we need to choose α, λ, and γ. For the latter two, we can perform a random search for hyper-parameters, as we discuss below. For the former, a parsimonious choice would be $\alpha = 1$, corresponding to a Laplace prior on the first temporal derivative of the latent code. For natural data, a value of $\alpha = 0.5$ would provide a better fit to Fig. 1, but a Laplace prior also achieves the goal of breaking the general rotation symmetry by having an optimum for axis-aligned representations, which is a requirement for identifiability. Therefore, we chose $\alpha = 1$ for this study. We derive a closed-form expression of the resulting KL in Appendix B.2.

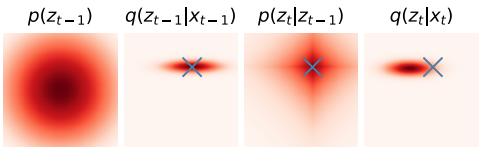

Figure 3: **SlowVAE illustration.** The prior and posterior for a two-dimensional latent space. Left to right: Normal prior for $t-1$, posterior for $t-1$, conditional Laplace prior for t, and posterior for t. The blue cross in the right three plots indicates the mean of the posterior for $t-1$.

3.4 Towards an Approximate Theory of Disentanglement

A number of our theoretical assumptions are violated in practice: After non-convex optimization, on a finite data sample, the distributions $p(\mathbf{x}_t, \mathbf{x}_{t-1})$ and $p^*(\mathbf{x}_t, \mathbf{x}_{t-1})$ are probably not perfectly matched. In addition, the model assumptions on $p(\mathbf{z}_t, \mathbf{z}_{t-1})$ likely do not fully match the distribution of the ground truth factors. For example, the model may be misspecified such that $\alpha \neq \alpha^*$ or $\lambda \neq \lambda^*$, or the chosen family of distributions may be incorrect altogether. In the following section we will present results on several datasets where the marginal distributions $p(\mathbf{z}_{t-1})$ are drawn from a Uniform (not Normal) distribution, and some of them are over unordered sets (categories) or bounded periodic spaces (rotation). Also, in practice the model latent space is usually chosen to have more dimensions than the ground truth generative model. On real data, factors of variation may be dependent (c.f. Träuble et al., 2020; Yang et al., 2020). Furthermore, the hypothesis class $\mathcal{G}$ of learnable functions in the VAE architecture may not contain the invertible ground truth generator $g^* \notin \mathcal{G}$. We note understanding the impact of these violations as an important focus area for continued progress towards developing a practical yet theoretically supported method for disentanglement on natural scenes.

4 Datasets with Natural Transitions

While the standard datasets compiled by DisLib are an important step towards real-world applications, they still assume the data is *i.i.d.*, which is decidedly untrue for natural data. As described in section 2, (Locatello et al., 2020) proposed uniformly sampling the number of factors to be changed, k, and changing said factors by uniformly sampling over the possible set of values. We enforce that k factors are changed for each transition, and refer to this data as "UNI". Considering our natural data analysis presented in Figure 1, such transitions are certainly unnatural.

Given the current state of evaluation, we provide a set of incrementally more complex datasets that we propose should be included in the standard benchmark suite to indicate how disentanglement approaches will scale towards natural data. Specifically, we construct datasets with (1) imposed sparse transitions, (2) augmented with natural continuous generative factors using measurements from unstructured natural videos, as well as (3) data from unstructured natural videos themselves, but provided in segmentation mask form to ensure visual complexity manageable for current methods. For the provided datasets, the object categories never change across transitions – reflecting natural object permanence. We summarize our contributed progression of increasingly complex and more natural datasets below, for further details, please refer to Appendix F).

Laplace Transitions (LAP) is a procedure for constructing image pairs from DisLib datasets by sampling from a conditional distribution shown to fit natural transitions well. For each ground-truth factor, the first value in the pair is chosen *i.i.d.* from the dataset and the second is chosen by weighting nearby factor values using Laplace distributed probabilities. If all factors remain constant (no transition), the sample is rejected as the pair would not result in any temporal learning signal. **Natural Sprites** consists of pairs of sprite images rendered from a distribution augmented by sampling from natural statistics. For a given image pair, the position and scale of the sprites are set using measured values from adjacent time points for unique entities present in YouTube-VOS. The sprite shapes are simple, like dSprites, and, along with orientation, are fixed for a given pair. We additionally consider a version of the dataset discretized to the granularity of dSprites, allowing us to leverage the standard DisLib metrics for evaluation (see Appendix F.3 for details). **KITTI Masks** is composed of pedestrian segmentation masks from an autonomous driving vision benchmark KITTI-MOTS, thus with natural shapes and continuous natural transitions in all underlying factors. We consider adjacent frames ($\Delta t = 1$), as well as frames with a temporal gap ($\Delta t = 5$).

5 Experiments

5.1 Empirical Studies

We evaluate models using the DisLib implementation for the following supervised metrics: BetaVAE (Higgins et al., 2017); FactorVAE (Kim and Mnih, 2018); Mutual Information Gap (MIG, (Chen et al., 2018)); Disentanglement, Compactness, and Informativeness (DCI [Disentanglement], (Eastwood and Williams, 2018)); Modularity (Ridgeway and Mozer, 2018); and Separated Attribute Predictability (SAP, (Kumar et al., 2018)) (see Appendix D for metric details). None of the DisLib metrics support ground-truth labels with continuous variation, which is required for evaluation on the continuous Natural Sprites and KITTI Masks datasets. To reconcile this, we measure the Mean Correlation Coefficient (MCC), a standard metric in the ICA literature that is applicable to continuous variables. We report mean and standard deviation across 10 random seeds and bold-face significant (independent T-test, $p < 0.05$) improvements between models.

In order to select the conditional prior regularization and the prior rate in an unsupervised manner, we perform a random search over $\gamma \in [1, 16]$ and $\lambda \in [1, 10]$ and compute the recently proposed unsupervised disentanglement ranking (UDR) scores (Duan et al., 2020). We notice that the optimal values are close to $\gamma = 10$ and $\lambda = 6$ on most datasets, and thus use these values for all experiments. We leave finding optimal values for specific datasets to future work, but note that it is a strong advantage of our approach that it works well with the same model specification across 14 datasets (counting LAP and UNI for DisLib, optional discretization for Natural Sprites, as well as different values for Δt with KITTI Masks), addressing a concern posed in (Locatello et al., 2018). Additional details on model selection and training can be found in Appendix E.2. For all visualizations, we pick the models with the highest average score across the DisLib metrics.

5.2 Results on DisLib and New Benchmarks

Our proposed model requires pairs for the training data provided in DisLib, although we show through evaluation with LAP and UNI that the specified conditional does not need to exactly match our theoretical assumptions. However, we do not need paired data points at test time, and thus it is possible to evaluate our model against previous *i.i.d.* approaches. In Table 1 we demonstrate favorable performance when compared to state of the art methods from nonlinear ICA (Hyvärinen et al., 2018) and disentanglement (Locatello et al., 2020) which leverage non-*i.i.d.* nature of the data for identifiability. In appendix H, we report results from a large-scale empirical test across metrics, datasets, and models to demonstrate that our model is superior in almost all settings.

Model	Data	MCC
PCL	Natural (Continuous)	51.7 (3.0)
Ada-GVAE	Natural (Continuous)	48.4 (4.8)
SlowVAE	Natural (Continuous)	49.1 (4.0)
PCL	Kitti ($\Delta t = 1$)	52.6 (5.1)
Ada-GVAE	Kitti ($\Delta t = 1$)	62.6 (7.5)
SlowVAE	Kitti ($\Delta t = 1$)	66.1 (4.5)
PCL	Kitti ($\Delta t = 5$)	58.5 (3.3)
Ada-GVAE	Kitti ($\Delta t = 5$)	67.6 (6.7)
SlowVAE	Kitti ($\Delta t = 5$)	**79.6** (5.8)

Table 2: Continuous ground-truth variable datasets. See Table 1 for details.

Model	Data	BetaVAE	FactorVAE	MIG	MCC	DCI	Modularity	SAP
PCL	dSprites (Uniform)	80.1 (0.4)	62.1 (0.9)	16.0 (7.4)	41.6 (1.5)	42.4 (1.2)	**99.7** (0.6)	6.0 (2.7)
Ada-GVAE	dSprites (Uniform)	88.0 (2.7)	73.1 (3.9)	17.3 (4.7)	46.0 (4.8)	32.3 (4.6)	93.3 (1.8)	6.6 (2.0)
SlowVAE	dSprites (Uniform)	87.0 (5.1)	75.2 (11.1)	**28.3** (11.5)	**58.8** (8.9)	47.7 (8.5)	86.9 (2.8)	4.4 (2.0)
PCL	dSprites (Laplace)	99.9 (0.1)	94.7 (3.1)	19.2 (3.1)	67.9 (3.3)	52.0 (3.5)	93.2 (0.9)	8.1 (1.6)
Ada-GVAE	dSprites (Laplace)	91.4 (1.6)	83.0 (5.9)	21.8 (4.9)	56.9 (4.2)	39.0 (4.2)	87.6 (1.8)	7.2 (0.3)
SlowVAE	dSprites (Laplace)	100.0 (0.0)	97.5 (3.0)	**29.5** (9.3)	69.8 (2.3)	**65.4** (3.6)	**96.5** (1.6)	8.1 (3.0)
PCL	Natural (Discrete)	82.4 (6.7)	68.3 (8.0)	7.8 (2.8)	50.2 (4.2)	14.3 (3.0)	88.9 (3.1)	2.5 (1.1)
Ada-GVAE	Natural (Discrete)	83.4 (1.1)	74.8 (4.4)	14.5 (3.2)	51.6 (2.5)	21.8 (2.9)	87.8 (2.5)	5.3 (1.4)
SlowVAE	Natural (Discrete)	82.6 (2.2)	76.2 (4.8)	11.7 (5.0)	52.6 (4.1)	18.9 (5.5)	88.1 (3.6)	4.4 (2.3)

Table 1: Mean and standard deviation (s.d.) metric scores across 10 random seeds. PCL is a scaled-up implementation of the method described by Hyvärinen and Morioka (2017), leveraging the encoding architecture and training hyperparameters specified in appendix E.2. Ada-GVAE is the leading method proposed by Locatello et al. (2020). Bold indicates statistical significance above the next highest score (independent T-test, $p < 0.05$). Red indicates statistical significance below the next lowest score. Results for additional datasets and models are in Table 2 and Appendix H.

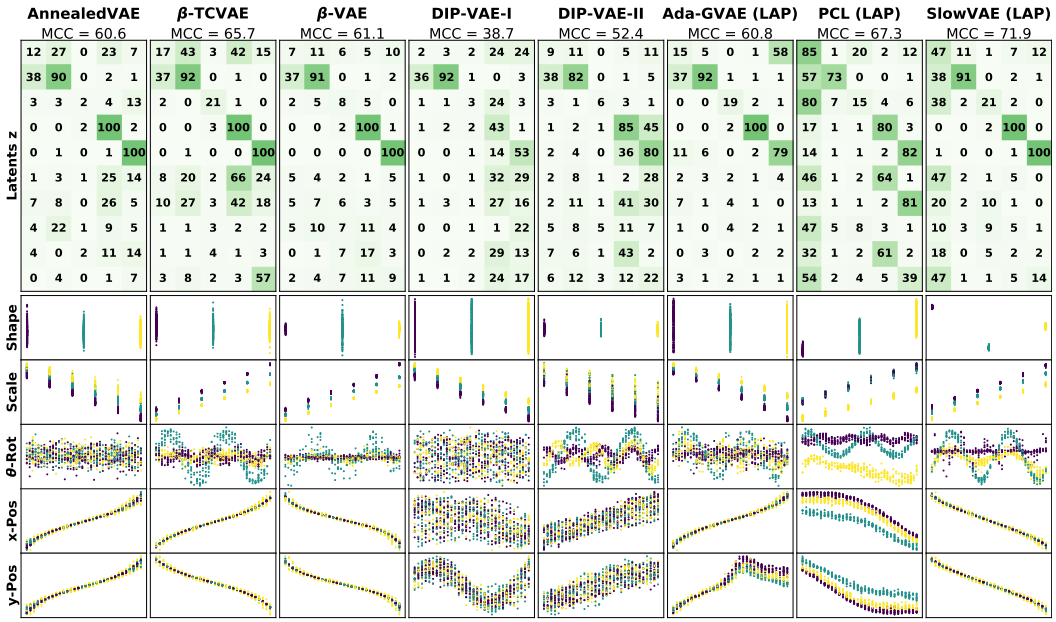

Figure 4: **DSprites Latent Representations:** (Top) shows absolute MCC between generative and model factors (rows are rearranged for maximal correlation on the main diagonal). The columns correspond to (shape, scale, rotation, x/y-position) and the values correspond to percent correlation. A more diagonal structure in the upper half corresponds to a better one-to-one mapping between generative and latent factors. (Bottom) shows individual latent dimensions (y-axis) over the matched generative factors (x-axis). Colors encode shapes: heart/yellow, ellipse/turquoise and square/purple.

Specifically, SlowVAE trained on UNI outperforms the previous state of the art in a majority of metrics on four out of the five benchmark datasets, with large gains specifically on dSprites, Shapes3D, and MPI3D. As expected, SlowVAE also performs better with the LAP dataset variant, which is better matched to the model assumptions, than the UNI dataset variant on almost datasets and metrics. We outperform β-VAE, which was chosen as representative of previous *i.i.d.* approaches, on all contributed datasets and metrics ($\beta = 8$, selected via UDR). On the KITTI Masks dataset, one source of variation in the data source is the parameter that determines the temporal distance between sampled frames. We run two settings ($\Delta t = 1$, $\Delta t = 5$) and observe that the benefit of temporal information is more apparent at $\Delta t = 5$ (Table 2). This links to recent work by Tschannen et al. (2019), who show that temporal separation between frame embeddings influences the representation that is learned from videos. In Fig. 5, we can see that the SlowVAE has learned latent dimensions which have correspondence with the estimated ground truth factors of x/y-position and scale.

Locatello et al. (2018) showed that all *i.i.d.* models performed similarly across the DisLib datasets and metrics when testing was carefully controlled. However, in Fig. 4 we observe that the different modeling assumptions result in differences in representation quality. To construct the visuals, we first compute the sorted correlation coefficient matrix between the latents and generative factors, which we visualize in the top row. The correlation matrix is sorted via linear sum assignment such that each ground-truth factor is non-greedily associated with the latent variable with highest correlation. Each row of scatter plots corresponds to an individual generative factor. In each subplot, the horizontal axis indicates the ground truth value, the vertical axis indicates the corresponding latent value, and the colors indicate object shape. These plots aid in understanding how each ground-truth factor is encoded in the latent space in a way that is more informative than exclusively visualizing latent traversals or embeddings of pairs of latent units (Cheung et al., 2014; Chen et al., 2016; Szabó et al., 2017; Ma et al., 2018). For example, in the third row, we observe that SlowVAE trained on UNI shows three sinusoidal oscillations with equal phase, but frequencies $\sim \omega, 2\omega,$ and 4ω, which correspond to the three distinct rotational symmetries of the shapes: heart, ellipse and square. We also note that the two datasets where we see the smallest performance differences (SmallNORB, Cars3D) have significantly more discrete categories $(50, 183)$ than the other datasets $(3 - 6)$. This could also explain why all models perform comparably on the Natural Sprites datasets, where unlike KITTI Masks the ground truth evaluation includes categorical and angular variables. As can be seen in Figure 4, such variables give all methods trouble, denoting an aspect of evaluation which future work can focus on improving performance with respect to.

Figure 5: **KITTI Masks.** (Left) MCC correlation matrix of the top 3 latents corresponding to y-position, x-position and scale. (Right) Images produced by varying the SlowVAE ($\Delta t = 5$) latent unit that corresponds to the corresponding row in the MCC matrix.

6 Conclusion

We provide evidence to support the hypothesis that natural scenes exhibit highly sparse transition probabilities, which we then leverage to contribute a novel nonlinear ICA framework that is provably identifiable up to permutations and sign-flips – a stronger result than has been achieved previously. With the SlowVAE model we provide a parsimonious implementation that is inspired by a long history of learning visual representations from temporal data (Hinton, 1990; Földiák, 1991). We apply this model to the current metric-based disentanglement benchmarks and it outperforms existing approaches (Locatello et al., 2020; Hyvärinen et al., 2018) on aggregate across almost all metrics and datasets without any tuning of its hyperparameters to individual datasets. Additionally, we provide a benchmark of novel video datasets to guide disentanglement research towards more natural domains. Going beyond KITTI Masks, which is constrained, YouTube-VOS is a large-scale, unstructured, natural dataset with a sufficient number of samples to alleviate overfitting concerns. The Natural Sprites dataset serves as a tractable bridge to facilitate progress on the way to the more challenging YouTube-VOS. Taken together, our dataset and model proposals set the stage for utilizing knowledge of natural scene statistics to advance unsupervised disentangled representation learning.

In our experiments we see that approximate identification as measured by the different disentanglement metrics increases despite violations of theoretical assumptions, which is in line with prior studies (Shu et al., 2019; Khemakhem et al., 2020; Locatello et al., 2020). Nevertheless, future work should address gaining a better understanding of the theoretical and empirical consequences of such model misspecifications, in order to make the theory of disentanglement more predictive about empirically found solutions.

REFERENCES

Tameem Adel, Zoubin Ghahramani, and Adrian Weller. Discovering interpretable representations for both deep generative and discriminative models. In *International Conference on Machine Learning*, pages 50–59, 2018.

Jonathan T Barron and Jitendra Malik. Shape, albedo, and illumination from a single image of an unknown object. In *2012 IEEE Conference on Computer Vision and Pattern Recognition*, pages 334–341. IEEE, 2012.

Anthony J Bell and Terrence J Sejnowski. An information-maximization approach to blind separation and blind deconvolution. *Neural Computation*, 7(6):1129–1159, 1995.

Yoshua Bengio, Aaron Courville, and Pascal Vincent. Representation learning: A review and new perspectives. *IEEE transactions on pattern analysis and machine intelligence*, 35(8):1798–1828, 2013.

Matthias Bethge. Factorial coding of natural images: how effective are linear models in removing higher-order dependencies? *JOSA A*, 23(6):1253–1268, 2006.

Christopher M Bishop. *Pattern recognition and machine learning*. springer, 2006.

Samuel R. Bowman, L. Vilnis, Oriol Vinyals, Andrew M. Dai, R. Józefowicz, and S. Bengio. Generating sentences from a continuous space. In *CoNLL*, 2016.

Christopher P Burgess, Irina Higgins, Arka Pal, Loic Matthey, Nick Watters, Guillaume Desjardins, and Alexander Lerchner. Understanding disentangling in beta-vae. *arXiv preprint arXiv:1804.03599*, 2018.

Richard H Byrd, Peihuang Lu, Jorge Nocedal, and Ciyou Zhu. A limited memory algorithm for bound constrained optimization. *SIAM Journal on scientific computing*, 16(5):1190–1208, 1995.

Charles F Cadieu and Bruno A Olshausen. Learning intermediate-level representations of form and motion from natural movies. *Neural Computation*, 24(4):827–866, 2012.

Tian Qi Chen, Xuechen Li, Roger B Grosse, and David K Duvenaud. Isolating sources of disentanglement in variational autoencoders. In *Advances in Neural Information Processing Systems*, pages 2610–2620, 2018.

Xi Chen, Yan Duan, Rein Houthooft, John Schulman, Ilya Sutskever, and Pieter Abbeel. Infogan: Interpretable representation learning by information maximizing generative adversarial nets. In *Advances in neural information processing systems*, pages 2172–2180, 2016.

Brian Cheung, Jesse A Livezey, Arjun K Bansal, and Bruno A Olshausen. Discovering hidden factors of variation in deep networks. *arXiv preprint arXiv:1412.6583*, 2014.

Pierre Comon. Independent component analysis, a new concept? *Signal processing*, 36(3):287–314, 1994.

Elliot Creager, David Madras, Jörn-Henrik Jacobsen, Marissa A Weis, Kevin Swersky, Toniann Pitassi, and Richard Zemel. Flexibly fair representation learning by disentanglement. In *International Conference on Machine Learning*, page 1436–1445, 2019.

Emily L Denton and Vighnesh Birodkar. Unsupervised learning of disentangled representations from video. In *Advances in Neural Information Processing Systems*, pages 4414–4423, 2017.

Adji B. Dieng, Yoon Kim, Alexander M. Rush, and D. Blei. Avoiding latent variable collapse with generative skip models. *ArXiv*, abs/1807.04863, 2019.

Laurent Dinh, David Krueger, and Yoshua Bengio. Nice: Non-linear independent components estimation. *ArXiv*, abs/1410.8516, 2017a.

Laurent Dinh, Jascha Sohl-Dickstein, and S. Bengio. Density estimation using real nvp. *ArXiv*, abs/1605.08803, 2017b.

Sunny Duan, Loic Matthey, Andre Saraiva, Nick Watters, Christopher Burgess, Alexander Lerchner, and Irina Higgins. Unsupervised model selection for variational disentangled representation learning. In *International Conference on Learning Representations (ICLR)*, 2020.

Cian Eastwood and Christopher KI Williams. A framework for the quantitative evaluation of disentangled representations. In *In International Conference on Learning Representations*, 2018.

Peter Földiák. Learning invariance from transformation sequences. *Neural Computation*, 3(2):194–200, 1991.

Lijian Gao, Qirong Mao, Ming Dong, Yu Jing, and Ratna Chinnam. On learning disentangled representation for acoustic event detection. In *Proceedings of the 27th ACM International Conference on Multimedia*, pages 2006–2014, 2019.

Andreas Geiger, Philip Lenz, and Raquel Urtasun. Are we ready for autonomous driving? the kitti vision benchmark suite. In *Conference on Computer Vision and Pattern Recognition (CVPR)*, 2012.

Muhammad Waleed Gondal, Manuel Wuthrich, Djordje Miladinovic, Francesco Locatello, Martin Breidt, Valentin Volchkov, Joel Akpo, Olivier Bachem, Bernhard Schölkopf, and Stefan Bauer. On the transfer of inductive bias from simulation to the real world: a new disentanglement dataset. In *Advances in Neural Information Processing Systems*, pages 15714–15725, 2019.

Will Grathwohl and Aaron Wilson. Disentangling space and time in video with hierarchical variational auto-encoders. *arXiv preprint arXiv:1612.04440*, 2016.

Luigi Gresele, Giancarlo Fissore, Adrian Javaloy, Bernhard Scholkopf, and Aapo Hyvarinen. Relative gradient optimization of the jacobian term in unsupervised deep learning. *ArXiv*, abs/2006.15090, 2020.

Wakako Hashimoto. Quadratic forms in natural images. *Network: Computation in Neural Systems*, 14(4): 765–788, 2003.

Junxian He, Daniel Spokoyny, Graham Neubig, and Taylor Berg-Kirkpatrick. Lagging inference networks and posterior collapse in variational autoencoders. *arXiv preprint arXiv:1901.05534*, 2019.

Irina Higgins, Loic Matthey, Arka Pal, Christopher Burgess, Xavier Glorot, Matthew Botvinick, Shakir Mohamed, and Alexander Lerchner. beta-vae: Learning basic visual concepts with a constrained variational framework. *International Conference on Learning Representations (ICLR)*, 2(5):6, 2017.

Irina Higgins, David Amos, David Pfau, Sebastien Racaniere, Loic Matthey, Danilo Rezende, and Alexander Lerchner. Towards a definition of disentangled representations. *arXiv preprint arXiv:1812.02230*, 2018.

Geoffrey E Hinton. Connectionist learning procedures. In *Machine learning*, page 208. Elsevier, 1990.

Aapo Hyvärinen and Patrik Hoyer. Emergence of phase-and shift-invariant features by decomposition of natural images into independent feature subspaces. *Neural computation*, 12(7):1705–1720, 2000.

Aapo Hyvärinen and Hiroshi Morioka. Unsupervised feature extraction by time-contrastive learning and nonlinear ica. In *Advances in Neural Information Processing Systems*, pages 3765–3773, 2016.

Aapo Hyvärinen and Hiroshi Morioka. Nonlinear ica of temporally dependent stationary sources. In *Proceedings of Machine Learning Research*, 2017.

Aapo Hyvärinen and Petteri Pajunen. Nonlinear independent component analysis: Existence and uniqueness results. *Neural Networks*, 12(3):429–439, 1999.

Aapo Hyvärinen, Jarmo Hurri, and Jaakko Väyrynen. Bubbles: a unifying framework for low-level statistical properties of natural image sequences. *JOSA A*, 20(7):1237–1252, 2003.

Aapo Hyvärinen, Hiroaki Sasaki, and Richard E Turner. Nonlinear ica using auxiliary variables and generalized contrastive learning. *arXiv preprint arXiv:1805.08651*, 2018.

Christian Jutten and Jeanny Herault. Blind separation of sources, part i: An adaptive algorithm based on neuromimetic architecture. *Signal Processing*, 24(1):1–10, 1991.

Ilyes Khemakhem, Diederik P Kingma, and Aapo Hyvärinen. Variational autoencoders and nonlinear ica: A unifying framework. *International Conference on Artificial Intelligence and Statistics (AISTATS)*, 2020.

Hyunjik Kim and Andriy Mnih. Disentangling by factorising. *arXiv preprint arXiv:1802.05983*, 2018.

Diederik P Kingma and Max Welling. Auto-encoding variational bayes. *arXiv preprint arXiv:1312.6114*, 2013.

Durk P Kingma and Prafulla Dhariwal. Glow: Generative flow with invertible 1x1 convolutions. In *Advances in neural information processing systems*, pages 10215–10224, 2018.

Durk P Kingma, Tim Salimans, Rafal Jozefowicz, Xi Chen, Ilya Sutskever, and Max Welling. Improved variational inference with inverse autoregressive flow. In *Advances in neural information processing systems*, pages 4743–4751, 2016.

Tejas D Kulkarni, William F Whitney, Pushmeet Kohli, and Josh Tenenbaum. Deep convolutional inverse graphics network. In *Advances in neural information processing systems*, pages 2539–2547, 2015.

Abhishek Kumar, Prasanna Sattigeri, and Avinash Balakrishnan. Variational inference of disentangled latent concepts from unlabeled observations. In *International Conference on Learning Representations*, 2018.

Yann LeCun, Fu Jie Huang, and Leon Bottou. Learning methods for generic object recognition with invariance to pose and lighting. In *Proceedings of the 2004 IEEE Computer Society Conference on Computer Vision and Pattern Recognition, 2004. CVPR 2004.*, volume 2, pages II–104. IEEE, 2004.

Francesco Locatello, Stefan Bauer, Mario Lucic, Gunnar Rätsch, Sylvain Gelly, Bernhard Schölkopf, and Olivier Bachem. Challenging common assumptions in the unsupervised learning of disentangled representations. *arXiv preprint arXiv:1811.12359*, 2018.

Francesco Locatello, Gabriele Abbati, Thomas Rainforth, Stefan Bauer, Bernhard Schölkopf, and Olivier Bachem. On the fairness of disentangled representations. In *Advances in Neural Information Processing Systems*, pages 14611–14624, 2019.

Francesco Locatello, Ben Poole, Gunnar Rätsch, Bernhard Schölkopf, Olivier Bachem, and Michael Tschannen. Weakly-supervised disentanglement without compromises. *arXiv preprint arXiv:2002.02886*, 2020.

James Lucas, George Tucker, Roger B Grosse, and Mohammad Norouzi. Don't blame the elbo! a linear vae perspective on posterior collapse. In *Advances in Neural Information Processing Systems*, pages 9408–9418, 2019.

Liqian Ma, Qianru Sun, Stamatios Georgoulis, Luc Van Gool, Bernt Schiele, and Mario Fritz. Disentangled person image generation. In *Proceedings of the IEEE Conference on Computer Vision and Pattern Recognition*, pages 99–108, 2018.

Lars Maaløe, Marco Fraccaro, Valentin Liévin, and Ole Winther. Biva: A very deep hierarchy of latent variables for generative modeling. In *Advances in neural information processing systems*, pages 6551–6562, 2019.

Emile Mathieu, Tom Rainforth, N Siddharth, and Yee Whye Teh. Disentangling disentanglement in variational autoencoders. In *Proceedings of the 36th International Conference on Machine Learning*, pages 4402–4412, 2019.

Loic Matthey, Irina Higgins, Demis Hassabis, and Alexander Lerchner. dsprites: Disentanglement testing sprites dataset. https://github.com/deepmind/dsprites-dataset/, 2017.

Stanisław Mazur and Stanisław Ulam. Sur les transformations isométriques d'espaces vectoriels normés. *CR Acad. Sci. Paris*, 194(946-948):116, 1932.

Anton Milan, Laura Leal-Taixé, Ian Reid, Stefan Roth, and Konrad Schindler. MOT16: A benchmark for multi-object tracking. *arXiv:1603.00831 [cs]*, March 2016.

Graeme Mitchison. Removing time variation with the anti-hebbian differential synapse. *Neural Computation*, 3 (3):312–320, 1991.

Hossein Mobahi, Ronan Collobert, and Jason Weston. Deep learning from temporal coherence in video. In *Proceedings of the 26th Annual International Conference on Machine Learning*, pages 737–744, 2009.

Hiroshi Morioka. Time-contrastive learning (tcl), 2018. URL `https://github.com/hirosm/TCL`.

Bruno A Olshausen. Learning sparse, overcomplete representations of time-varying natural images. In *Proceedings 2003 International Conference on Image Processing (Cat. No. 03CH37429)*, volume 1, pages I–41. IEEE, 2003.

Adam Paszke, Sam Gross, Francisco Massa, Adam Lerer, James Bradbury, Gregory Chanan, Trevor Killeen, Zeming Lin, Natalia Gimelshein, Luca Antiga, et al. Pytorch: An imperative style, high-performance deep learning library. In *Advances in Neural Information Processing Systems*, pages 8024–8035, 2019.

F. Pedregosa, G. Varoquaux, A. Gramfort, V. Michel, B. Thirion, O. Grisel, M. Blondel, P. Prettenhofer, R. Weiss, V. Dubourg, J. Vanderplas, A. Passos, D. Cournapeau, M. Brucher, M. Perrot, and E. Duchesnay. Scikit-learn: Machine learning in Python. *Journal of Machine Learning Research*, 12:2825–2830, 2011.

Scott E Reed, Yi Zhang, Yuting Zhang, and Honglak Lee. Deep visual analogy-making. In *Advances in neural information processing systems*, pages 1252–1260, 2015.

Karl Ridgeway. A survey of inductive biases for factorial representation-learning. *arXiv preprint arXiv:1612.05299*, 2016.

Karl Ridgeway and Michael C Mozer. Learning deep disentangled embeddings with the f-statistic loss. In *Advances in Neural Information Processing Systems*, pages 185–194, 2018.

Michal Rolinek, Dominik Zietlow, and Georg Martius. Variational autoencoders pursue pca directions (by accident). In *Proceedings of the IEEE Conference on Computer Vision and Pattern Recognition*, pages 12406–12415, 2019.

Rui Shu, Yining Chen, Abhishek Kumar, Stefano Ermon, and Ben Poole. Weakly supervised disentanglement with guarantees. *arXiv preprint arXiv:1910.09772*, 2019.

Eero P Simoncelli and Bruno A Olshausen. Natural image statistics and neural representation. *Annual review of neuroscience*, 24(1):1193–1216, 2001.

Fabian Sinz, Sebastian Gerwinn, and Matthias Bethge. Characterization of the p-generalized normal distribution. *Journal of Multivariate Analysis*, 100(5):817–820, 2009.

Jascha Sohl-Dickstein, Ching Ming Wang, and Bruno A Olshausen. An unsupervised algorithm for learning lie group transformations. *arXiv preprint arXiv:1001.1027*, 2010.

Peter Sorrenson, Carsten Rother, and Ulrich Kothe. Disentanglement by nonlinear ica with general incompressible-flow networks (gin). *ArXiv*, abs/2001.04872, 2017.

Attila Szabó, Qiyang Hu, Tiziano Portenier, Matthias Zwicker, and Paolo Favaro. Challenges in disentangling independent factors of variation. *arXiv preprint arXiv:1711.02245*, 2017.

Esteban G Tabak and Cristina V Turner. A family of nonparametric density estimation algorithms. *Communications on Pure and Applied Mathematics*, 66(2):145–164, 2013.

Esteban G Tabak, Eric Vanden-Eijnden, et al. Density estimation by dual ascent of the log-likelihood. *Communications in Mathematical Sciences*, 8(1):217–233, 2010.

Frederik Träuble, Elliot Creager, Niki Kilbertus, Anirudh Goyal, Francesco Locatello, Bernhard Schölkopf, and Stefan Bauer. Is independence all you need? on the generalization of representations learned from correlated data. *arXiv preprint arXiv:2006.07886*, 2020.

Michael Tschannen, Josip Djolonga, Marvin Ritter, Aravindh Mahendran, Neil Houlsby, Sylvain Gelly, and Mario Lucic. Self-supervised learning of video-induced visual invariances. *arXiv preprint arXiv:1912.02783*, 2019.

Richard Turner and Maneesh Sahani. A maximum-likelihood interpretation for slow feature analysis. *Neural computation*, 19(4):1022–1038, 2007.

Paul Voigtlaender, Michael Krause, Aljosa Osep, Jonathon Luiten, Berin Balachandar Gnana Sekar, Andreas Geiger, and Bastian Leibe. Mots: Multi-object tracking and segmentation. *Conference on Computer Vision and Pattern Recognition (CVPR)*, 2019.

Nicholas Watters, Loic Matthey, Sebastian Borgeaud, Rishabh Kabra, and Alexander Lerchner. Spriteworld: A flexible, configurable reinforcement learning environment, 2019. URL `https://github.com/deepmind/spriteworld/`.

Laurenz Wiskott and Terrence J Sejnowski. Slow feature analysis: Unsupervised learning of invariances. *Neural Computation*, 14(4):715–770, 2002.

Ning Xu, Linjie Yang, Yuchen Fan, Dingcheng Yue, Yuchen Liang, Jianchao Yang, and Thomas Huang. Youtube-vos: A large-scale video object segmentation benchmark. *arXiv preprint arXiv:1809.03327*, 2018.

Linjie Yang, Yuchen Fan, and Ning Xu. Video instance segmentation. *arXiv preprint arXiv:1905.04804*, 2019.

Mengyue Yang, Furui Liu, Zhitang Chen, Xinwei Shen, Jianye Hao, and Jun Wang. Causalvae: Structured causal disentanglement in variational autoencoder. *arXiv preprint arXiv:2004.08697*, 2020.

Ilker Yildirim, Mario Belledonne, Winrich Freiwald, and Josh Tenenbaum. Efficient inverse graphics in biological face processing. *Science Advances*, 6(10):eaax5979, 2020.

Will Zou, Shenghuo Zhu, Kai Yu, and Andrew Y Ng. Deep learning of invariant features via simulated fixations in video. In *Advances in neural information processing systems*, pages 3203–3211, 2012.

APPENDIX

A Broader Impact **14**

B Formal Methods **14**

B.1 Proof of Identifiability 14

B.2 Kullback Leibler Divergence of Slow Variational Autoencoder 16

C Choosing a Latent Variable Model **17**

D Disentanglement Metrics **19**

D.1 Mean Correlation Coefficient 19

D.2 DisLib Metrics 19

E Estimation Methods **21**

E.1 Model Training and Selection 21

E.2 Implementation Details 21

F Natural Datasets **21**

F.1 Laplace Transitions 21

F.2 YouTube-VOS 22

F.3 Natural Sprites 22

F.4 KITTI MOTS Pedestrian Masks 23

G Extended Comparison to Similar Methods **24**

G.1 Theoretical Comparison 24

G.2 Empirical Comparison 25

H Additional Results **26**

H.1 Extended Data Analysis 26

H.2 All DisLib Results 26

H.3 Latent Space Visualizations 28

A BROADER IMPACT

Representation learning is at the heart of model building for cognition. Our specific contribution is focused on core methods for modeling natural videos and the datasets used are more simplistic than real-world examples. However, foundational research on unsupervised representation learning has potentially large impact on AI for advancing the power of self-learning systems.

The broader field of representation learning has a large number of focused research directions that span machine learning and computational neuroscience. As such, the application space for this work is vast. For example, applications in unsupervised analysis of complicated and unintuitive data, such as medical imaging and gene expression information, have great potential to solve fundamental problems in health sciences. A future iteration of our disentangling approach could be used to encode such complicated data into a lower-dimensional and more understandable space that might reveal important factors of variation to medical researchers. Another important and complex modeling space that could potentially be improved by this line of research is in environmental sciences and combating global climate change.

Nonetheless, we acknowledge that any machine learning method can be used for nefarious purposes, which can be mitigated via effective, scientifically informed communication, outreach, and policy direction. We unconditionally denounce the use of derivatives of our work for weaponized or wartime applications. Additionally, due to the lack of interpretability generally found in modern deep learning approaches, it is possible for practitioners to inadvertently introduce harmful biases or errors in machine learning applications. Although we certainly do not solve this problem, our focus on providing identifiable solutions to representation learning is likely beneficial for both interpretability and fairness in machine learning.

B FORMAL METHODS

Function / variable	Description
g	Generator
α	Prior shape
λ	Prior rate
$p(\mathbf{z})$	Prior
$\mathbf{z} \sim p(\mathbf{z})$	Latent variables
$\mathbf{x} = g(\mathbf{z})$	Generated images
$q(\mathbf{z}\|\mathbf{x})$	Variational posterior

Table 3: Glossary of terms. We use a * (i.e. g^*) when necessary to highlight that we are referring to the ground truth model.

B.1 PROOF OF IDENTIFIABILITY

To study disentanglement, we assume that the generative factors $\mathbf{z} \in \mathbb{R}^D$ are mapped to images $\mathbf{x} \in \mathbb{R}^N$ (usually $D << N$) by a nonlinear ground-truth generator $g^* : \mathbf{z} \mapsto \mathbf{x}$. We consider a representation with a learned generator g *disentangled* if it inverts the ground-truth generator in the sense that the composition $\sigma = (g^*)^{-1} \circ g$ can be described by a simple permutation and sign flips.

Theorem 1 *For a ground-truth $(g^*, \lambda^*, \alpha^*)$ and a learned (g, λ, α) generative model as defined in equation (2), if the following assumptions are satisfied:*

- *The generators g^* and g are defined everywhere in the latent space. Moreover, they are injective and differentiable almost everywhere,*
- *There is no model misspecification i.e. $\alpha = \alpha^*$ and $\lambda = \lambda^*$, so $\mathbf{z} \sim p(\mathbf{z}) = p^*(\mathbf{z})$,*
- *Pairs of images are generated as $(\mathbf{x}^*_{t-1}, \mathbf{x}^*_t) = (g^*(\mathbf{z}_{t-1}), g^*(\mathbf{z}_t))$ and $(\mathbf{x}_{t-1}, \mathbf{x}_t) = (g(\mathbf{z}_{t-1}), g(\mathbf{z}_t))$,*

- *The distributions of* $(\mathbf{x}^*_{t-1}, \mathbf{x}^*_t)$ *and* $(\mathbf{x}_{t-1}, \mathbf{x}_t)$ *are the same (i.e. the corresponding densities are equal almost everywhere:* $p^*(\mathbf{x}_{t-1}, \mathbf{x}_t) = p(\mathbf{x}_{t-1}, \mathbf{x}_t)$*,*

then $g = g^* \circ \sigma$*, where* σ *is a composition of a permutation and sign flips.*

Proof. Since $\mathbf{x} = g(\mathbf{z})$ can be written as $\mathbf{x} = (g^* \circ (g^*)^{-1} \circ g)(\mathbf{z})$, we can assume that $g = g^* \circ h$ for some function h on the latent space.

We first show that the function h is a bijection on the latent space. It is injective, since both g and g^* are injective. If it were not surjective, there would be a point $\tilde{\mathbf{z}}$ in the ground-truth latent space, which would not have a pre-image under h. Because of continuity of h, there would be some neighborhood $\mathbf{U}_{\tilde{\mathbf{z}}}$ of $\tilde{\mathbf{z}}$ which would not have a pre-image under h. That would mean that images generated by g^* from $\mathbf{U}_{\tilde{\mathbf{z}}}$ would have zero density under the distribution of images generated by g (i.e. $p(g^*(\mathbf{U}_{\tilde{\mathbf{z}}})) = 0$), while this density would be non-zero under the distribution of images directly generated by the ground-truth generator g^* (i.e. $p^*(g^*(\mathbf{U}_{\tilde{\mathbf{z}}})) \neq 0$), which contradicts the assumption that these distributions are equal. It follows that h is bijective.

In the next step, we show that the distribution of latent space pairs $(h(\mathbf{z}_{t-1}), h(\mathbf{z}_t))$ matches the latent space prior distribution (i.e. h preserves the prior distribution in the latent space). Indeed, using the assumption that the distributions of $(g^*(\mathbf{z}_{t-1}), g^*(\mathbf{z}_t))$ and $((g^* \circ h)(\mathbf{z}_{t-1}), (g^* \circ h)(\mathbf{z}_t))$ are the same, we can write the following equality using the change of variables formula:

$$\begin{aligned} p^*(\mathbf{x}_{t-1}, \mathbf{x}_t) &= p((g^*)^{-1}(\mathbf{x}_{t-1}), (g^*)^{-1}(\mathbf{x}_t)) \left| \det \left(\frac{\mathrm{d}(g^*)^{-1}}{\mathrm{d}(\mathbf{x}_{t-1}, \mathbf{x}_t)} \right) \right| \\ &= p_h((g^*)^{-1}(\mathbf{x}_{t-1}), (g^*)^{-1}(\mathbf{x}_t)) \left| \det \left(\frac{\mathrm{d}(g^*)^{-1}}{\mathrm{d}(\mathbf{x}_{t-1}, \mathbf{x}_t)} \right) \right| = p(\mathbf{x}_{t-1}, \mathbf{x}_t), \end{aligned} \tag{5}$$

where p and p_h are densities of $(\mathbf{z}_{t-1}, \mathbf{z}_t)$ and $(h(\mathbf{z}_{t-1}), h(\mathbf{z}_t))$. Since the determinants above cancel, these densities are equal at the pre-image of any pair of images $(\mathbf{x}_{t-1}, \mathbf{x}_t)$. Because g^* is defined everywhere in the latent space, p and p_h are equal for any pair of latent space points. Applying the change of variables formula again, we obtain the following equation:

$$\begin{aligned} &p(\mathbf{z}_{t-1}, \mathbf{z}_t) = p(h^{-1}(\mathbf{z}_{t-1}), h^{-1}(\mathbf{z}_t)) \left| \det \left(\frac{\mathrm{d}h^{-1}}{\mathrm{d}(\mathbf{z}_{t-1}, \mathbf{z}_t)} \right) \right| \\ &= p(h^{-1}(\mathbf{z}_{t-1}))\, p(h^{-1}(\mathbf{z}_t) \mid h^{-1}(\mathbf{z}_{t-1})) \left| \det \left(\frac{\mathrm{d}h^{-1}(\mathbf{z}_{t-1})}{\mathrm{d}\mathbf{z}_{t-1}} \right) \right| \left| \det \left(\frac{\mathrm{d}h^{-1}(\mathbf{z}_t)}{\mathrm{d}\mathbf{z}_t} \right) \right| \\ &= p(\mathbf{z}_{t-1})\, p(\mathbf{z}_t \mid \mathbf{z}_{t-1}). \end{aligned} \tag{6}$$

Note that the probability measure p is the same before and after the change of variables, since we showed that the prior distribution in the latent space must be invariant under the function h. The same condition for the marginal $p(\mathbf{z}_{t-1})$ is as follows:

$$p(\mathbf{z}_{t-1}) = p(h^{-1}(\mathbf{z}_{t-1})) \left| \det \left(\frac{\mathrm{d}h^{-1}(\mathbf{z}_{t-1})}{\mathrm{d}\mathbf{z}_{t-1}} \right) \right|. \tag{7}$$

Solving for the determinant of the Jacobian in (7) and plugging it into (6), we obtain

$$p(\mathbf{z}_t \mid \mathbf{z}_{t-1}) = p(h^{-1}(\mathbf{z}_t) \mid h^{-1}(\mathbf{z}_{t-1})) \frac{p(\mathbf{z}_t)}{p(h^{-1}(\mathbf{z}_t))}. \tag{8}$$

Taking logs of both sides, we arrive at the following equation:

$$A(||\mathbf{z}_t - \mathbf{z}_{t-1}||_\alpha^\alpha - ||h^{-1}(\mathbf{z}_t) - h^{-1}(\mathbf{z}_{t-1})||_\alpha^\alpha) = B(||\mathbf{z}_t||_2^2 - ||h^{-1}(\mathbf{z}_t)||_2^2), \tag{9}$$

where A and B are the constants appearing in the exponentials in $p(\mathbf{z}_{t-1})$ and $p(\mathbf{z}_t \mid \mathbf{z}_{t-1})$. The logs of normalization constants cancel out.

For any $\mathbf{z}_t$ we can choose $\mathbf{z}_{t-1} = \mathbf{z}_t$ making the left hand side in (9) equal to zero. This implies that $||\mathbf{z}_t||_2^2 = ||h^{-1}(\mathbf{z}_t)||_2^2$ for any $\mathbf{z}_t$, i.e. function h^{-1} preserves the 2-norm. Moreover, the preservation of the 2-norm implies that $p(\mathbf{z}_{t-1}) = p(h^{-1}(\mathbf{z}_{t-1}))$ and therefore it follows from (7) that for any $\mathbf{z}$

$$\left| \det \left(\frac{\mathrm{d}h^{-1}(\mathbf{z})}{\mathrm{d}\mathbf{z}} \right) \right| = 1. \tag{10}$$

Thus, the left hand side of (9) can be re-written as

$$||\mathbf{z}_t - \mathbf{z}_{t-1}||_\alpha^\alpha - ||h^{-1}(\mathbf{z}_t) - h^{-1}(\mathbf{z}_{t-1})||_\alpha^\alpha = 0. \tag{11}$$

This means that h^{-1} preserves the α-distances between points. Moreover, because h is bijective, the Mazur-Ulam theorem (Mazur and Ulam, 1932) tells us that h must be an affine transform.

In the next step, to prove that h must be a permutation and sign flip, let us choose an arbitrary point $\mathbf{z}_{t-1}$ and $\mathbf{z}_t = \mathbf{z}_{t-1} + \varepsilon\, \mathbf{e}_k = (z_{1,1}, \ldots, z_{1,k} + \varepsilon, \ldots, z_{1,D})$. Using (11) and performing a Taylor expansion around $\mathbf{z}_{t-1}$, we obtain the following:

$$\begin{aligned}
\varepsilon^\alpha &= ||\mathbf{z}_t - \mathbf{z}_{t-1}||_\alpha^\alpha \\
&= ||h^{-1}(\mathbf{z}_{t-1} + \varepsilon\, \mathbf{e}_k) - h^{-1}(\mathbf{z}_{t-1})||_\alpha^\alpha \\
&= \left|\left|\varepsilon \cdot \left(\frac{\partial h_1^{-1}(\mathbf{z}_{t-1})}{z_{t-1,k}}, \ldots, \frac{\partial h_D^{-1}(\mathbf{z}_{t-1})}{z_{t-1,k}}\right) + O(\varepsilon^2)\right|\right|_\alpha^\alpha.
\end{aligned} \tag{12}$$

The higher-order terms $O(\varepsilon^2)$ are zero since h is affine, therefore dividing both sides of the above equation by ε^α we find that

$$\left|\left|\left(\frac{\partial h_1^{-1}(\mathbf{z}_{t-1})}{z_{t-1,k}}, \ldots, \frac{\partial h_D^{-1}(\mathbf{z}_{t-1})}{z_{t-1,k}}\right)\right|\right|_\alpha^\alpha = 1. \tag{13}$$

The vectors of k-th partial derivatives of components of h^{-1} are columns of the Jacobian matrix $\left(\frac{\mathrm{d}h^{-1}(\mathbf{z})}{\mathrm{d}\mathbf{z}}\right)$. Using the fact that the determinant of that matrix is equal to one and applying Hadamard's inequality, we obtain that

$$\left|\det\left(\frac{\mathrm{d}h^{-1}(\mathbf{z})}{\mathrm{d}\mathbf{z}}\right)\right| = 1 \leq \prod_{k=1}^{D} \left|\left|\left(\frac{\partial h_1^{-1}(\mathbf{z}_{t-1})}{z_{t-1,k}}, \ldots, \frac{\partial h_D^{-1}(\mathbf{z}_{t-1})}{z_{t-1,k}}\right)\right|\right|_2. \tag{14}$$

Since $\alpha < 2$, for any vector $\mathbf{v}$ it holds that $||\mathbf{v}||_2 \leq ||\mathbf{v}||_\alpha$, with equality only if at most one component of $\mathbf{v}$ is non-zero. This inequality implies that both (13) and (14) hold at the same time if and only if

$$\left|\left|\left(\frac{\partial h_1^{-1}(\mathbf{z}_{t-1})}{z_{t-1,k}}, \ldots, \frac{\partial h_D^{-1}(\mathbf{z}_{t-1})}{z_{t-1,k}}\right)\right|\right|_2 = \left|\left|\left(\frac{\partial h_1^{-1}(\mathbf{z}_{t-1})}{z_{t-1,k}}, \ldots, \frac{\partial h_D^{-1}(\mathbf{z}_{t-1})}{z_{t-1,k}}\right)\right|\right|_\alpha = 1, \tag{15}$$

meaning that only one element of these vectors of k-th partial derivatives is non-zero, and it is equal to 1 or -1. Thus, the function h is a composition of a permutation and sign flips at every point. Potentially, this permutation might be input-dependent, but we argued above that h is affine, therefore the permutation must be the same for all points. □

B.2 Kullback Leibler Divergence of Slow Variational Autoencoder

The VAE learns a variational approximation to the true posterior by maximizing a lower bound on the log-likelihood of the empirical data distribution $\mathcal{D}$

$$\begin{aligned}
&E_{\mathbf{x}_{t-1},\mathbf{x}_t \sim \mathcal{D}}[\log p(\mathbf{x}_{t-1}, \mathbf{x}_t)] \geq \\
&\quad E_{\mathbf{x}_{t-1},\mathbf{x}_t \sim \mathcal{D}}[E_{q(\mathbf{z}_t,\mathbf{z}_{t-1}|\mathbf{x}_t,\mathbf{x}_{t-1})}[\log p(\mathbf{x}_{t-1}, \mathbf{x}_t, \mathbf{z}_{t-1}, \mathbf{z}_t) - \log q(\mathbf{z}_t, \mathbf{z}_{t-1}|\mathbf{x}_t, \mathbf{x}_{t-1})]].
\end{aligned} \tag{16}$$

For this, we need to compute the Kullback-Leibler divergence (KL) between the posterior $q(\mathbf{z}_t, \mathbf{z}_{t-1}|\mathbf{x}_t, \mathbf{x}_{t-1})$ and the prior $p(\mathbf{z}_t, \mathbf{z}_{t-1})$. Since all of these distributions are per design factorial, we will, for simplicity, derive the KL below for scalar variables (log-probabilities will simply have to be summed to obtain the full expression). Recall that the model prior and posterior factorize like

$$\begin{aligned}
p(z_t, z_{t-1}) &= p(z_t|z_{t-1})\, p(z_{t-1}) \\
q(z_t, z_{t-1}|\mathbf{x}_t, \mathbf{x}_{t-1}) &= q(z_t|\mathbf{x}_t)\, q(z_{t-1}|\mathbf{x}_{t-1}).
\end{aligned} \tag{17}$$

Then, given a pair of inputs $(\mathbf{x}_{t-1}, \mathbf{x}_t)$, the KL can be written

$$\begin{aligned}
&D_{KL}(q(z_t, z_{t-1}|\mathbf{x}_t, \mathbf{x}_{t-1})|p(z_t, z_{t-1})) = E_{z_t, z_{t-1}\sim q(z_t, z_{t-1}|\mathbf{x}_t, \mathbf{x}_{t-1})}\left[\log \frac{q(z_t|\mathbf{x}_t)\, q(z_{t-1}|\mathbf{x}_{t-1})}{p(z_t|z_{t-1})\, p(z_{t-1})}\right] \\
&= E_{z_{t-1}\sim q(z_{t-1}|\mathbf{x}_{t-1})}\left[\log \frac{q(z_{t-1}|\mathbf{x}_{t-1})}{p(z_{t-1})}\right] + E_{z_t, z_{t-1}\sim q(z_t, z_{t-1}|\mathbf{x}_t, \mathbf{x}_{t-1})}\left[\log \frac{q(z_t|\mathbf{x}_t)}{p(z_t|z_{t-1})}\right] \\
&= D_{KL}(q(z_{t-1}|\mathbf{x}_{t-1})|p(z_{t-1})) - H(q(z_t|\mathbf{x}_t)) + E_{z_{t-1}\sim q(z_{t-1}|\mathbf{x}_{t-1})}\left[H(q(z_t|\mathbf{x}_t), p(z_t|z_{t-1}))\right]
\end{aligned} \tag{18}$$

Where we use the fact that KL divergences decompose like $D_{KL}(X, Y) = H(X, Y) - H(X)$ into (differential) cross-entropy $H(X, Y)$ and entropy $H(X)$. The first term of the last line in (18) is the same KL divergence as in the standard VAE, namely between a Gaussian distribution $q(z_{t-1}|\mathbf{x}_{t-1})$ with some $\mu(\mathbf{x}_{t-1})$ and $\sigma(\mathbf{x}_{t-1})$ and a standard Normal distribution $p(z_{t-1})$. The solution of the KL is given by $D_{KL}(q(z_{t-1}|\mathbf{x}_{t-1})|q(z_{t-1})) = -\log \sigma(\mathbf{x}_{t-1}) + \frac{1}{2}(\mu(\mathbf{x}_{t-1})^2 + \sigma(\mathbf{x}_{t-1})^2 - 1)$ (Bishop, 2006). The second term on the RHS, i.e. the entropy of a Gaussian is simply given by $H(q(z_t|\mathbf{x}_t)) = \log(\sigma(\mathbf{x}_t)\sqrt{2\pi e})$.

To compute the last term on the RHS, let us recall the Laplace form of the conditional prior

$$p(z_t|z_{t-1}) = \frac{\lambda}{2} \exp -\lambda|z_t - z_{t-1}|. \tag{19}$$

Thus the cross-entropy becomes

$$\begin{aligned}
H(q(z_t|\mathbf{x}_t), p(z_t|z_{t-1})) &= -E_{z_t\sim q(z_t|\mathbf{x}_t)}[\log p(z_t|z_{t-1})] \\
&= -\log\left(\frac{\lambda}{2}\right) + \lambda E_{z_t\sim q(z_t|\mathbf{x}_t)}[|z_t - z_{t-1}|].
\end{aligned} \tag{20}$$

Now, if some random variable $X \sim \mathcal{N}(\mu,\, \sigma^2)$, then $Y = |X|$ follows a *folded normal distribution*, for which the mean is defined as

$$E[|x|] = \sigma\sqrt{\frac{2}{\pi}} \exp\left(-\frac{\mu^2}{2\sigma^2}\right) - \mu\left(1 - 2\,\Phi\left(\frac{\mu}{\sigma}\right)\right), \tag{21}$$

where Φ is the cumulative distribution function of a standard normal distribution (mean zero and variance one). Thus, denoting $\mu(\mathbf{x}_t, z_{t-1}) = \mu(\mathbf{x}_t) - z_{t-1}$, we can rewrite further

$$\begin{aligned}
&H(q(z_t|\mathbf{x}_t), p(z_t|z_{t-1})) = \\
&-\log\left(\frac{\lambda}{2}\right) + \lambda\left(\sigma(\mathbf{x}_t)\sqrt{\frac{2}{\pi}} \exp\left(-\frac{\mu(\mathbf{x}_t, z_{t-1})^2}{2\sigma(\mathbf{x}_t)^2}\right) - \mu(\mathbf{x}_t, z_{t-1})\left(1 - 2\,\Phi\left(\frac{\mu(\mathbf{x}_t, z_{t-1})}{\sigma(\mathbf{x}_t)}\right)\right)\right).
\end{aligned} \tag{22}$$

C Choosing a Latent Variable Model

Our proposed method for disentanglement can be implemented in conjunction with different probabilistic latent variable models. In this section, we compare VAEs and normalizing flows as possible candidates.

Variational Autoencoders (VAEs) (Kingma and Welling, 2013) are a widely used probabilistic latent variable model. Despite their simple structure and empirical success, VAEs can converge to a pathological solution called *posterior collapse* (Lucas et al., 2019; Bowman et al., 2016; He et al.,

2019). This solution results in the encoder's variational posterior approximation matching the prior, which is typically chosen to be a multivariate standard normal $q_\phi(\mathbf{z}|\mathbf{x}^*) \approx p(\mathbf{z}) = \mathcal{N}(\mathbf{0}, \mathbf{I})$. This disconnects the encoder from the decoder, making them approximately independent, i.e. $p_\theta(\mathbf{x}|\mathbf{z}) \approx p_\theta(\mathbf{x})$. The failure mode is often observed when the decoder architecture is overly expressive, i.e. with autoregressive models, or when the evidence $p^*(\mathbf{x})$ is easy to estimate. Approaches that alleviate this problem rely on modifying the ELBO training objective (Bowman et al., 2016; Kingma et al., 2016) or restricting the decoder structure (Dieng et al., 2019; Maaløe et al., 2019). However, these approaches come with various drawbacks, including optimization issues (Lucas et al., 2019).

Another approach to estimate latent variables are normalizing flows which describe a sequence of invertible mappings by iteratively applying the change of variables rule (Dinh et al., 2017b). Unlike VAEs, flow based latent variable models allow for a direct optimization of the evidence $p^*(\mathbf{x})$ (Dinh et al., 2017b). Most normalizing flow models rely on a fast and reliable calculation of the determinant of the Jacobian of the outputs with respect to the inputs, which constrains the architectural design and limits the capacity of the network (Tabak et al., 2010; Tabak and Turner, 2013; Dinh et al., 2017b). Thus, competitive flows require very deep architectures in practice (Kingma and Dhariwal, 2018). Furthermore, flows are not directly suited for a scenario where the observation space is higher dimensional than the generating latent factors, $\dim(\mathbf{z}^*) << \dim(\mathbf{x}^*)$, as the computation of the determinant requires a square Jacobian matrix. We tried setting the number of dimensions of the observation space equal to the number of dimensions in the latent space $dim(\mathbf{z}) = dim(\mathbf{x}) >> dim(\mathbf{z}^*)$, but observed instability while optimizing the objective defined below.

It is straight forward to derive a flow based objective based on the assumptions in equation (2). We consider a normalizing flow with with K blocks $f(\mathbf{x}) = f_K \circ ... \circ f_1 : \mathbf{x} \mapsto \mathbf{z}$. The coupling blocks can refer to nonlinear mixing similar to Kingma and Dhariwal (2018), or in the linear case ($K = 1$) to an invertible de-mixing matrix. This leads to the following estimation of the data probability

$$p(\mathbf{x}_{t-1}, \mathbf{x}_t) = \; p(f(\mathbf{x}_{t-1}))\; p(f(\mathbf{x}_t)|f(\mathbf{x}_{t-1}))\; \prod_{k=1}^{K} \left|\det \frac{\partial f_k}{\partial \mathbf{z}_{k-1,t-1}}\right|^{-1} \prod_{k=1}^{K} \left|\det \frac{\partial f_k}{\partial \mathbf{z}_{k-1,t}}\right|^{-1}. \tag{23}$$

Note that $p(f(\mathbf{x}_{t-1}))$ is Gaussian and $p(f(\mathbf{x}_t)|f(\mathbf{x}_{t-1}))$ is a Laplacian, similar to equation (2). For notation convenience, we also introduced $\mathbf{z}_0 = \mathbf{x}^*$. During optimization we take the $-\log$ of both sides and minimize w.r.t. the parameters of f. We refer to this estimator as *SlowFlow*. Next, we compare SlowFlow and SlowVAE in the context of disentanglement.

To demonstrate the posterior collapse in VAEs, we generate data points (x_t, x_{t-1}) according to equation (2) with a two dimensional latent space $\dim(\mathbf{z}^*) = 2$. We consider a trivial linear mixing of $\mathbf{x}^* = \mathbf{W}^*\mathbf{z}^* = g^*(\mathbf{z}^*)$ with

$$\mathbf{W}^* = \text{diag}(1, \kappa) \tag{24}$$

and $\kappa \in [0.1, 1]$. As can be seen by looking at the σ and μ outputs of the encoder in Fig 6, for $\kappa < 0.4$, the encoder $q_\phi(z_0|\mathbf{x})$ collapses to the prior $p(z_0)$. The decoder then tries minimize the reconstruction loss by solely covering the main principal component of the data, which is also described in Rolinek et al. (2019). Despite the collapse and decrease in MCC, the SlowVAE loss from equation (4) still improves during training. On the other hand, a simple linear SlowFlow model $f(\mathbf{x}) = \mathbf{W}\mathbf{x}$, which directly optimizes the evidence $p^*(\mathbf{x})$, recovers the latents consistently as seen by the MCC measure.

To show the strength of the VAE model we increase the complexity of the data-distribution by using a non-linear expanding decoder such that $\dim(\mathbf{x}^*) >> \dim(\mathbf{z}^*)$. In Fig. 7 we observe that increasing the input dimensionality is sufficient for SlowVAE to find the corresponding latents and achieve high MCC with low loss.

Each estimation method is practically useful in different experimental settings. In the case when the mixing operation is trivially defined (equation (24), or when the number of dimensions in Z^* match those in X^*, the VAE estimator tends to learn a pathological solution. On the other hand, the normalizing flow estimator does not scale well to high data dimensions due to the requirement of computing the network Jacobian. Additionally, the framework for constructing normalizing flow estimators assumes the latent dimensionality is equal to the data dimensionality to allow for an invertible transform. Together these results lead us to choose an estimator based on the nature of the problem. For our contributing datasets and the DisLib experiments we adopt the VAE framework.

However, if one aims to perform simplified experiments such as those typically conducted in the nonlinear ICA literature, it often will make practical sense to switch to a flow-based estimator.

D DISENTANGLEMENT METRICS

Several recent studies have brought to light shortcomings in a number of proposed disentanglement metrics (Kim and Mnih, 2018; Eastwood and Williams, 2018; Chen et al., 2018; Higgins et al., 2018; Mathieu et al., 2019), many of which have been compiled in the DisLib benchmark. In addition to the concerns they raise, it is important to note that none of the supervised metrics implemented in DisLib allow for continuous ground-truth factors, which is necessary for evaluating with the Natural Sprites and KITTI Masks datasets, as factors such as position and scale are effectively continuous in reality. To rectify this issue without introducing novel metrics, we include the Mean Correlation Coefficient (MCC) as implemented by Hyvärinen and Morioka (2016), which is described below.

We measure all metrics presented below between $10,000$ samples of latent factors $\mathbf{z}$ and the corresponding encoded means of our model $\mu(g^*(\mathbf{z}))$. We increase this sample size to $100,000$ for Modularity and MIG to stabilize the entropy estimates.

D.1 MEAN CORRELATION COEFFICIENT

In addition to the DisLib metrics, we also compute the Mean Correlation Coefficient (MCC) in order to perform quantitative evaluation with continuous variables. Because of Theorem 1, perfect disentanglement in the noiseless case should always lead to a correlation coefficient of 1 or -1, although note that we report 100 times the absolute value of the correlation coefficient. In our experiments, MCC is used without modification from the authors' open-sourced code (Morioka, 2018). The method first measures correlation between the ground-truth factors and the encoded latent variables. The initial correlation matrix is then used to match each latent unit with a preferred ground-truth factor. This is an assignment problem that can be solved in polynomial time via the Munkres algorithm, as described in the code release (Morioka, 2018). After solving the assignment problem, the correlation coefficients are computed again for the vector of ground-truth factors and the resulting permuted vector of latent encodings, where the output is a matrix of correlation coefficients with D columns for each ground-truth factor and D' rows for each latent variable. We use the (absolute value of the) Spearman coefficient as our correlation measure which assumes a monotonic relationship between the ground-truth factors and latent encodings but tolerates deviations from a strictly linear correspondence.

In the existing implementation for MCC, the ground truth factors, latent encodings, and mixed signal inputs are assumed to have the same dimensionality, i.e. $D = D' = N$. However, in our case, the ground-truth generating factors are much lower dimensional than the signal, $N << D$, and the latent encoding is higher dimensional than the ground-truth factors $D' > D$ (see Appendix E.2 for details). To resolve this discrepancy, we add $D' - D$ standard Gaussian noise channels to the ground-truth factors. To compute the MCC score, we take the mean of the absolute value of the upper diagonal of the correlation matrix. The upper diagonal is the diagonal of the square matrix of D ground-truth factors by the top D most correlated latent dimensions after sorting. In this way, we obtain an MCC estimate which averages only over the D correlation coefficients of the D ground truth factors with their corresponding best matching latent factors,

D.2 DISLIB METRICS

BetaVAE (Higgins et al., 2017)

BetaVAE uses a biased estimator with tunable hyperparameters, although we follow the convention established in (Locatello et al., 2018) of using the *scikit-learn* defaults. For a sample in a batch, a pair of images, $(\mathbf{x}_1, \mathbf{x}_2)$, is generated by fixing the value of one of the data generative factors while uniformly sampling the rest. The absolute value of the difference between the latent codes produced from the image pairs is then taken, $\mathbf{z}_{\text{diff}} = |\mathbf{z}_1 - \mathbf{z}_2|$. A logistic classifier is fit with batches of $\mathbf{z}_{\text{diff}}$ variables and the corresponding index of the fixed ground-truth factor serves as the label. Once the classifier is trained, the metric itself is the mean classifier accuracy on a batch of held-out test data.

The training minimizes the following loss:

$$L = \frac{1}{2}\mathbf{w}^T\mathbf{w} + \sum_{i=1}^{n} \log(\exp(-\mathbf{y}_i(\mathbf{z}_{\text{diff},i}^T\mathbf{w} + c)) + 1), \tag{25}$$

where $\mathbf{w}$ and c are the learnable weight matrix and bias, respectively, and $\mathbf{y}$ is the index of the fixed ground-truth factor for the batch. The network is trained using the `lbfgs` optimizer (Byrd et al., 1995), which is implemented via the *scikit-learn* Python package (Pedregosa et al., 2011) in `disentanglement_lib` (Locatello et al., 2018). In the original work, the authors argue that their metric improves over a correlation metric such as the mean correlation coefficient by additionally measuring interpretability, although the linear operation of $\mathbf{z}_{\text{diff},i}^T\mathbf{w} + c$ can perform demixing, which means the measure gives no direct indication of identifiability and thus does not guarantee that the latent encodings are interpretable, especially in the case of dependent factors. Additionally, as noted by Kim and Mnih (2018), BetaVAE can report perfect accuracy when all but one of the ground-truth factors are disentangled, since the classifier can trivially attribute the remaining factor to the remaining latents.

FactorVAE (Kim and Mnih, 2018)

For FactorVAE, the variance of the latent encodings is computed for a large (10,000 in DisLib) batch of data where all factors could possibly be changing. Latent dimensions with variance below some threshold (0.05 in DisLib) are rejected and not considered further. Next, the encoding variance is computed again on a smaller batch (64 in DisLib) of data where one factor is fixed during sampling. The quotient of these two quantities (with the larger batch variance as the denominator) is then taken to obtain a normalized variance estimate per latent factor. Finally, a majority-vote classifier is trained to predict the index of the ground-truth factor with the latent unit that has the lowest normalized variance. The FactorVAE score is the classification accuracy for a batch of held-out data.

Mutual Information Gap (Chen et al., 2018)

The Mutual Information Gap (MIG) metric was introduced as an alternative to the classifier-based metrics that we discuss herein. It provides a normalized measure of the mean difference in mutual information between each ground truth factor and the two latent codes that have the highest mutual information with the given ground truth factor. As it is implemented in DisLib, MIG measures entropy by discretizing the model's latent code using a histogram with 20 bins equally spaced between the representation minimum and maximum. It then computes the discrete mutual information between the ground-truth values and the discretized latents using the *scikit-learn* `metrics.mutual_info_score` function (Pedregosa et al., 2011). For the normalization it divides this difference by the entropy of the discretized ground truth factors.

Modularity (Ridgeway and Mozer, 2018)

Ridgeway and Mozer (2018) measure disentanglement in terms of three factors: modularity, compactness, and explicitness. For modularity, they first measure the mutual information between the discretized latents and ground-truth factors using the same histogram procedure that was used for the MIG, resulting in a matrix, $M \in \mathbb{R}^{D' \times D}$ with entries for each mutual information pair. Their measure of modularity is then

$$\text{modularity} = \tfrac{1}{D'}\sum_{i=1}^{D'} \Theta\left(1 - \frac{\sum_{j=1}^{D} M_{i,j}^2 - \max(M_i^2)}{\max(M_i^2)(D-1)}\right), \tag{26}$$

where $\max(M_i^2)$ returns the maximum of the vector of squared mutual information measurements between ground truth i and each latent factor. Additionally, Θ is a selection function that returns zero for any i where $\max(M_i^2) = 0$ and otherwise acts as the identity function.

DCI Disentanglement (Eastwood and Williams, 2018)

The DCI scores measure disentanglement, completeness, and informativeness, which have intuitive correspondence to the modularity, compactness, and explicitness of (Ridgeway and Mozer, 2018), respectively. To measure DCI Disentanglement, D regressors are trained to predict each ground truth factor state given the latent encoding. The DisLib implementation uses the `ensemble.GradientBoostingClassifier` function from *scikit-learn* with default parameters, which trains D gradient boosted logistic regression tree classifiers. Importance is assigned

to each latent factor using the built-in `feature_importance_` property of the classifier, which computes the normalized total reduction of the classifier criterion loss contributed by each latent. Disentanglement is then measured as

$$\sum_{i=1} D(1 - H(I_i))\tilde{I}_i, \tag{27}$$

where H is the entropy computed with the `stats.entropy` function from *scikit-learn*, $I \in \mathbb{R}^{D \times D'}$ is a matrix of the absolute value of the feature importance between each factor and each ground truth, and $\tilde{I}$ is a normalized version of the matrix

$$\tilde{I}_i = \frac{\sum_{j=1}^{D'} I_{i,j}}{\sum_{k=1}^{D} \sum_{j=1}^{D'} I_{k,j}} \tag{28}$$

SAP Score (Kumar et al., 2018)

To compute the SAP score, Kumar et al. (2018) first train a linear support vector classifier with squared hinge loss and L_2 penalty to predict each ground truth factor from each latent variable. In DisLib this is implemented with the `svm.LinearSVC` function with default parameters from *scikit-learn*. They construct a score matrix $S \in \mathbb{R}^{D' \times D}$, where each entry in the matrix is the batch-mean classifier accuracy for predicting each ground truth given each individual latent encoding. For each generative factor, they compute the difference between the top two most predictive latent dimensions, which are the two highest scores in a given column of S. The mean (across ground-truth factors) of these differences is the SAP score.

E Estimation Methods

E.1 Model Training and Selection

We train all models on all datasets provided in DisLib with the **UNI** and **LAP** variants. We also train SlowVAE and β-VAE on **Natural Sprites** and **KITTI Masks**. When available, we compare scores directly using models we train, otherwise we reprint scores reported in (Locatello et al., 2020).

E.2 Implementation Details

All models are implemented in PyTorch (Paszke et al., 2019). To facilitate comparison, the training parameters, e.g. optimizer, batch size, number of training steps, as well as the VAE encoder and decoder architecture are identical to those reported in (Locatello et al., 2018; 2020). We use this architecture for all datasets, only adjusting the number of input channels (greyscale for dSprites, smallNORB, and KITTI Masks; three color channels for all other datasets).

The model formulation is agnostic to the direction of time. Therefore, to increase the temporal training signal at a fixed computational cost for each batch of input pairs $(\mathbf{x}_0, \mathbf{x}_1)$, we optimize the model in both directions i.e. optimizing the model objective for both $t_0 = 0$, $t_1 = 1$ as well as $t_0 = 1$, $t_1 = 0$.

F Natural Datasets

We introduce several datasets to investigate disentanglement in more natural scenarios. Here, we provide a detailed description on the design of each dataset.

F.1 Laplace Transitions

For each of the datasets in DisLib, we collect pairs of images. For each ground-truth factor, the first value in the pair is chosen from a uniform distribution across all possible values in latent space, while the second is chosen by weighting nearby values in latent space using Laplace distributed probabilities (see equation 2). Since we are restricted to the set of given factor values, the dataset has edge conditions where samples that would push a factor outside the preset range are rejected. This

may, however, alleviate issues introduced by rotation symmetries since, under this Laplace prior in the latent space, it is extremely unlikely to observe 'large' transitions from orientations of $\theta = 2\pi - \epsilon$ to $\theta = \epsilon$. This dataset introduces a hyper-parameter λ that controls the rate of the Laplace sampling distribution, while the location is set by the initial factor value. Effectively, when this rate is $\lambda = 1$ most of the factors change most of the time, whereas for a rate of $\lambda = 10$ most of the factors will not change most of the time (recall that we reject samples without any changes, so at least one factor will change in every valid sample). To maximize comparability with (Locatello et al., 2020), for each pair of inputs we sample the rate of the Laplace prior from a uniform distribution $\lambda \sim \mathcal{U}(1, 10)$. This correspond to the setting (k =rand) in the LOC data, which is reported throughout the paper.

F.2 YouTube-VOS

For the YouTube dataset, we download annotations from the 2019 version of the video instance segmentation (Youtube-VIS) dataset (Yang et al., 2019)[3], which is built on top of the video object segmentation (Youtube-VOS) dataset (Xu et al., 2018). The dataset has annotations for every five frames in a 30fps video, which results in a 6fps sampling rate. The authors believe that the temporal correlation between five consecutive frames is sufficiently strong that annotations can be omitted for intermediate frames to reduce the annotation efforts. Such a skip-frame annotation strategy enables scaling up the number of videos and objects annotated under the same budget, yielding 131,000 annotations for 2,883 videos, with 4,883 unique video object instances.

The original image size of the dataset is 720×1280. In order to preserve the statistics of the transitions, we choose not to directly downsample to 64×64, but instead preserve the aspect ratio by downsampling to 64×128. In order to minimize the bias yielded by the extraction method, noting the center bias typically present in human videos, we extract three equally spaced 64×64 pixel windows (with overlap) with a stride of 32.

For each resulting $64 \times 64 \times T$ sequence, where T denotes the number of time steps in the sequence, we filter out all pairs where the given object instance is not present in adjacent frames, resulting in 234,652 pairs.

An issue with evaluating disentanglement on natural datasets is the fact that the existing disentanglement metrics require knowledge of the underlying generative process of the given data. Although we can observe that the world is composed of distinct entities that vary according to rules imposed by physics, we are unable to determine the precise "factors" that generate such scenes. To mitigate this problem, we compile object measurements by calculating the x and y coordinates of the center of mass as well as the area of each object in each frame. We use these measurements to a) augment existing disentanglement benchmarks with natural transitions (Natural Sprites) and b) evaluate the ability of algorithms to decode intrinsic object properties (KITTI Masks).

F.3 Natural Sprites

Without a definition of disentanglement that can be applied to unknown data generating processes, we are limited to synthetic datasets with known ground-truth factors. Let us take dSprites (Matthey et al., 2017) as an example. The dataset consists of all combinations of a set of latent factor values, namely,

- Color: white
- Shape: square, ellipse, heart
- Scale: 6 values linearly spaced in $[0.5, 1]$
- Orientation: 40 values in $[0, 2\pi]$
- Position X: 32 values in $[0, 1]$
- Position Y: 32 values in $[0, 1]$

Given the limited set of discrete values each factor can take on, all possible samples can be described by a tractable dataset, compiled and released to the public. But, in reality, all of these factors should be continuous: a spectrum of possible colors, shapes, scales, orientations, and positions exist. We address this by constructing a dataset that is augmented with natural and continuous ground truth

[3] https://competitions.codalab.org/competitions/20127

Config	Scale	X	Y	(R, G, B)	Shape	Orientation
Continuous	YT [2375]	YT [197342]	YT [187112]	(1.0, 1.0, 1.0)	(square, triangle, star_4, spoke_4)	(0,9,...,342,351)
Discrete	YT [6]	YT [32]	YT [32]	(1.0, 1.0, 1.0)	(square, triangle, star_4, spoke_4)	(0,9,...,342,351)

Table 4: Natural Sprite Configs. Values in brackets refer to the number of unique values. Shapes presented are predefined in Spriteworld (Watters et al., 2019).

factors, using the mask properties measured from the large-scale, natural, unstructured YouTube (Xu et al., 2018; Yang et al., 2019) dataset.

We can choose the complexity of the dataset by discretizing the 234,652 transition pairs of position and scale into an arbitrary number of bins. In this study, we discretize to match dSprites, which we present in Table 4. We produce a pair by fixing the color, shape, and orientation, but updating the position and scale with transitions sampled from the YouTube measurements. To minimize the effect of extreme outliers, we filter out 10% of the data by removing frames if the mask area falls below the 5% or above the 95% quantiles, which reduces the number of pairs to 207,794. Finally, we use the Spriteworld (Watters et al., 2019) renderer to generate the images. The benchmark is available at `https://zenodo.org/record/3948069`.

In relation to the Laplace transitions described in section F.1, this update a) produces pairs that correspond to transitions observed in real data and b) allows for smooth transitions by defining the data generation process as opposed to being limited by the given collected dataset (e.g. dSprites). We generate the data online, thus training the model to fit the underlying distribution as opposed to a sampled finite dataset.

However, as noted previously, all supervised metrics aggregated in DisLib are inapplicable to continuous factors, which is problematic as the generating distribution is effectively continuous with respect to a subset of the factors. Therefore, we limit our quantitative evaluation to MCC for continuous datasets. Additionally, as mentioned above, to evaluate disentanglement with the standard metrics, we bin the collected transition statistics to match the size of dSprites and use the set of bin centers as the new set of values. The details of which are in Table 4, note that the discretization corresponds to the scale of the dSprites factor set.

F.4 KITTI MOTS Pedestrian Masks

While Natural Sprites enables evaluation of disentanglement with natural transitions, we note that the disentanglement framework which requires knowledge of the underlying generative factors is unrealistic for real-world data. As we state in the introduction, the assumption that a visual representation of the world can be constructed via a generative process that receives factors of variation as input and produces natural signals as output is not true in the literal sense. Measurements such as scale and position correspond to object properties that are ecologically relevant to the observer and can serve as suitable alternatives to the typical generative factors. We directly test this using our KITTI Masks dataset.

To create the dataset, we download annotations from the Multi-Object Tracking and Segmentation (MOTS) Evaluation Benchmark (Voigtlaender et al., 2019; Geiger et al., 2012; Milan et al., 2016), which is split into KITTI MOTS and MOTSChallenge[4]. Both datasets contain sequences of pedestrians with their positions densely annotated in the time and pixel domains. The original image sizes are 1080×1920 or 480×640 resolution for MOTSChallenge and between 370 and 374 pixels tall by 1224 and 1242 pixels wide for KITTI MOTS. For simplicity, we only consider the instance segmentation masks for pedestrians and do not use the raw data. We use nearest neighbor down-sampling for each frame such that the height was 64 pixels and the width is set to conserve the aspect ratio. After down-sampling, we use a horizontal sliding window approach to extract six equally spaced windows of size 64×64 (with overlap) for each sequence in both datasets. Note that here we make reasonable assumptions on horizontal translation and scale invariance of the dataset. We justify the assumed scale invariance by observing that the data is collected from a camera mounted onto a car which has varying distance to pedestrians. To confirm the translation invariance, we show an ablation study on the number of horizontal images. Instead of six horizontal, equally spaced sliding windows,

[4] `https://www.vision.rwth-aachen.de/page/mots`

we only use two which leads to differently placed windows. We do not observe significant changes in the reported data statistics (e.g. the kurtosis of the fit stays within $\pm 10\%$ of the previous value for Δx transitions). The values of Δy and $\Delta area$ do not change significantly compared to Table 6.

For each resulting $64 \times 64 \times T$ sequence, where T denotes the number of time steps in the sequence, we extract all individual pedestrian masks based on their object instance identity and create a new sequence for each pedestrian such that each resulting sequence only contains a single pedestrian. We ignore images with masks that have less than 30 pixels as they are too far away or occluded and not recognizable by humans. We keep all sequences of two or more frames, as the algorithm only requires pairs of frames for training.

The resulting **KITTI Masks** dataset consists of 2,120 sequences of individual pedestrians with lengths between 2 and 710 frames each, resulting in a total of 84,626 individual frames. We estimate ground truth factors by calculating the x and y coordinates of the center of mass of each pedestrian in each frame and the area (number of pixels in mask). We leave the Δt between time frames within a pair as a hyperparameter, and test $\Delta t = 1$ and $\Delta t = 5$ as described in the main paper. During training, we augment the data by applying horizontal and vertical translations of ± 5 pixels and rotations of $\pm 2^\circ$ degree. We apply the exact same data augmentation to both images within a pair to not change any transition statistics. For samples and the corresponding ground truth factors see Fig. 8. The benchmark is available at `https://zenodo.org/record/3931823`.

G Extended Comparison to Similar Methods

G.1 Theoretical Comparison

Nonlinear ICA has recently been advanced significantly by several papers from Hyvärinen and colleagues. Of these studies, the two that are most comparable to our work is Hyvärinen and Morioka (2017), which uses an unsupervised contrastive loss for nonlinear demixing and Khemakhem et al. (2020), which extends the nonlinear ICA framework to include variational autoencoders (VAEs). However, our theory covers an important class of transitions relevant for natural data that is not covered by the identifiability proofs of either of the aforementioned studies. Specifically, the non-Gaussian autoregressive model their identifiability proof rests upon (their equation (8)) assumes that the second derivative of the innovation probability density function is less than zero to satisfy *uniform dependence*, which is only met for $\alpha > 1$ for generalized Laplace transitions. While they denote (footnote 3) that Laplace distributions ($\alpha = 1$) are not covered by their theory, they offer a suggestion for a smooth approximation. However, they do not demonstrate that this approximation is useful in practice.

We chose a generalized Laplacian to fit our data and for our model assumption as it allows for simple parameterization of fits to data (e.g. $\alpha = 0.5$ for natural movie transitions), but is simultaneously quite expressive (Sinz et al., 2009). Though we use $\alpha = 1$ in practice for our estimation method, we prove identifiability up to permutations and sign flips for any $\alpha < 2$, covering all sparse distributions under the expressive generalized Laplacian model. Hyvärinen and Morioka (2017) do not provide a class of smooth approximations for $\alpha <= 1$, and thus their theory does not achieve the same ends. In addition, we assume a Gaussian marginal distribution that allows us to derive a fundamentally stronger proof of identifiability – where we identify up to permutation and sign-flips. Hyvärinen and Morioka (2017) only identify the sources up to arbitrary non-linear element-wise transformations. Thus they require a subsequent step of ICA recover the signal up to permutations and sign flips for a class of distributions where it is unclear whether they account for temporal sparsity.

This difference is also evident in the form of the conditional priors, $p(\mathbf{z}_t|\mathbf{z}_{t-1})$, used by us and by Khemakhem et al. (2020). They assume that the conditional posterior is part of the exponential family, but this does not include Laplacian conditionals. Even though the exponential family contains the Laplace distribution with fixed mean as its member, this does not allow their approach to model sparse transitions. They assume that the natural parameters of the exponential family distribution are conditioned on $\mathbf{z}_{t-1}$, meaning that only the scale but not the mean of the Laplace prior for $\mathbf{z}_t$ can be modulated by the previous time step, thus not allowing for sparse transition probabilities. Additionally, their implementation requires the number of classes (i.e. states of the conditioning variable) to equal the number of stationary segments, which is impractical for the datasets we consider.

Method	L=1	L=2	L=3	L=4	L=5
PCL	0.998	0.960	0.950	0.917	0.902
PCL (NF)	0.946	0.918	0.918	0.917	0.876
SlowFlow	**0.997**	**0.987**	**0.982**	**0.975**	**0.975**

Table 5: MCC using linear correlation where $L = x$ denotes the number of mixing layers.

Thus, we provide a closer match to natural data transitions, with a stronger identifiability result, as well as an implementation capable of scale when compared to previous nonlinear ICA approaches.We provide validation by performing an extensive evaluation leveraging our contributed datasets as well as the models, metrics, and datasets provided by the Disentanglement Library (discussed in section 4). We consider methods functionally capable of processing transitions from not only the disentanglement literature (Locatello et al., 2020), but that of nonlinear ICA (Hyvärinen and Morioka, 2017). As (Hyvärinen and Morioka, 2017), unlike (Hyvärinen and Morioka, 2016; Khemakhem et al., 2020), contributes a fitting model, we consider their simulation setting more carefully in the following section.

G.2 Empirical Comparison

Hyvärinen and Morioka (2017) conducted a simulation where the sources in the nonlinear ICA model come from a linear autoregressive (AR) model with non-Gaussian innovations. Specifically, temporally dependent 20-dimensional source signals were randomly generated according to $\log p(s(t)|s(t-1)) = -|s(t) - 0.7s(t-1)|$. Though this generative process was noted to not be covered by the theory presented in (Hyvärinen and Morioka, 2017), the authors demonstrated that PCL could reconstruct the source signals reasonably well even for the nonlinear mixture case. Given our practical use of a Laplacian conditional, we evaluated our theory in this artificial setting.

Given C, we use SlowFlow for these experiments. For computational tractability in demixing highly nonlinear transformations, we consider normalizing flows (Dinh et al., 2017a;b; Kingma and Dhariwal, 2018), namely volume-preserving flows (Sorrenson et al., 2017), as we find constraining the Jacobian determinant to stabilize learning. To ensure sufficient expressivity, we consider 6 coupling blocks, each containing a 2-layer MLP with 500 hidden units and ReLU nonlinearities. We compare to the PCL implementation presented in (Hyvärinen et al., 2018), where an MLP with the same number of hidden layers as the mixing MLP was adopted, where we use 100 hidden units as we did not find increasing the value improved performance. To account for the architectural difference serving as a possible confounder, we use the same encoder for optimizing the PCL objective, which we term "PCL (NF)".

While (Hyvärinen and Morioka, 2017) used leaky ReLU nonlinearities to make the mixing invertible, said mixing is non-differentiable. This is problematic for SlowFlow, as it involves gradient optimization of the Jacobian term, and more importantly, unlike PCL, aims to explicitly recover the mixing process. We thus use a a smooth version of the leaky-ReLU activation function with a hyperparameter α (Gresele et al., 2020),

$$\mathrm{s_L}(x) = \alpha x + (1-\alpha)\log(1+e^x). \tag{29}$$

By ensuring the mixing process is smooth, we find that SlowFlow performs favorably relative to PCL 5 when evaluated in the same setting, converging to a better optimum at higher levels of mixing.

dataset	N	Δ area	Δ x	Δ y
KITTI	82506	68.92	38.50	65.39
YouTube	234652	76.49	39.98	35.59

Table 6: Empirical estimates of Kurtosis for mask transitions per metric for each dataset.

dataset	N	genlaplace	normal	laplace
KITTI	82506	-3.21e+05	-3.79e+05	-3.35e+05
YouTube	234652	-1.29e+06	-1.45e+06	-1.33e+06

Table 7: Maximum likelihood scores for the considered distributions on Δ **area** for each dataset.

H ADDITIONAL RESULTS

H.1 EXTENDED DATA ANALYSIS

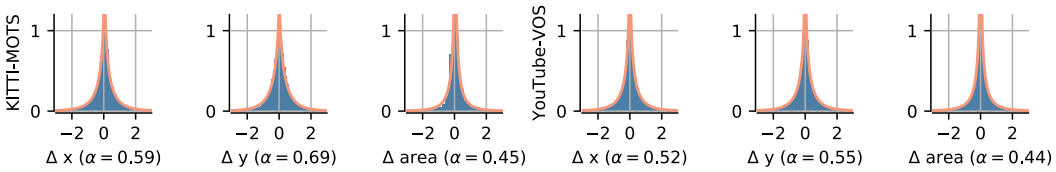

Figure 9: **Statistics of Natural Transitions**. Distribution over transitions for horizontal (Δx) and vertical (Δy) position as well as mask/object size ($\Delta area$) for both datasets. Red lines indicate fits of generalized Laplace distributions (equation (2)) and α is the shape value estimate.

We report the empirical estimates of Kurtosis in Table 6. We report the log-likelihood scores for the Δ area, Δ x, Δ y statistics in Tables 7, 8, and 9, respectively for a Normal, a Laplace and a generalized Laplace/Normal distribution. For these distributions, we also report the fit parameters for the Δ area, Δ x, Δ y statistics in Tables 10, 11, and 12, respectively, where the shape parameter α of the generalized Laplacian is bolded. As a higher likelihood indicates a better fit, we can see further evidence that natural transitions are highly leptokurtic; a Laplace distribution ($\alpha = 1$) is a better fit than a Gaussian ($\alpha = 2$), while the generalized Laplacian yields the highest likelihood consistently with $\alpha \approx 0.5$ for all measurements, as indicated in the main paper.

H.2 ALL DISLIB RESULTS

We include results on all DisLib datasets, dSprites (Matthey et al., 2017), Cars3D (Reed et al., 2015), SmallNORB (LeCun et al., 2004), Shapes3D (Kim and Mnih, 2018), MPI3D (Gondal et al., 2019), in Tables 13, 14, 15, 16, and 17, respectively. We report both median (a.d.) to compare to the previous median scores reported in (Locatello et al., 2020), as well as the the more common mean (s.d.) scores for future comparisons and straightforward statistical estimates of significant differences between models.

dataset	N	genlaplace	normal	laplace
KITTI	82506	-8.72e+04	-1.20e+05	-9.25e+04
YouTube	234652	-4.50e+05	-5.64e+05	-4.74e+05

Table 8: Maximum likelihood scores for the considered distributions on Δ **x** for each dataset.

dataset	N	genlaplace	normal	laplace
KITTI	82506	-7.59e+04	-1.07e+05	-7.86e+04
YouTube	234652	-4.40e+05	-5.45e+05	-4.60e+05

Table 9: Maximum likelihood scores for the considered distributions on Δ **y** for each dataset.

dataset	N	genlaplace	normal	laplace
KITTI	82506	[**4.55e-01**, 1.00e+00, 1.01e+00]	[4.53e-01, 2.39e+01]	[1.00e+00, 1.07e+01]
YouTube	234652	[**4.44e-01**, 1.47e-16, 5.04e+00]	[2.25e-01, 1.16e+02]	[7.73e-09, 5.28e+01]

Table 10: Parameter fits for the considered distributions on Δ **area** for each dataset. The parameters are (alpha, location, scale) for generalized Laplace/Normal, (location, scale) for the other two distributions.

dataset	N	genlaplace	normal	laplace
KITTI	82506	[**5.87e-01**, 4.76e-02, 1.69e-01]	[5.34e-02, 1.04e+00]	[5.49e-02, 5.64e-01]
YouTube	234652	[**5.15e-01**, 1.15e-14, 2.57e-01]	[2.32e-03, 2.68e+00]	[7.54e-09, 1.38e+00]

Table 11: Parameter fits for the considered distributions on Δ **x** for each dataset. The parameters are (alpha, location, scale) for generalized Laplace/Normal, (location, scale) for the other two distributions.

dataset	N	genlaplace	normal	laplace
KITTI	82506	[**6.94e-01**, 1.02e-02, 2.32e-01]	[3.84e-02, 8.86e-01]	[1.71e-02, 4.77e-01]
YouTube	234652	[**5.48e-01**, 2.93e-13, 3.08e-01]	[8.81e-03, 2.47e+00]	[9.15e-04, 1.30e+00]

Table 12: Parameter fits for the considered distributions on Δ **y** for each dataset. The parameters are (alpha, location, scale) for generalized Laplace/Normal, (location, scale) for the other two distributions.

Model (Data)	BetaVAE	FactorVAE	MIG	DCI	Modularity	SAP
β-VAE (*i.i.d.*)	82.3	66.0	10.2	18.6	82.2	4.9
Ada-ML-VAE (LOC)	89.6	70.1	11.5	29.4	89.7	3.6
Ada-GVAE (LOC)	92.3	84.7	26.6	47.9	91.3	7.4
SlowVAE (LOC)	89.7 (3.8)	81.4 (8.4)	34.5 (9.6)	50.0 (6.9)	87.1 (2.0)	5.1 (1.5)
SlowVAE (LAP)	100.0 (0.0)	99.2 (2.3)	28.2 (8.2)	65.5 (3.1)	96.8 (1.4)	6.0 (2.4)
SlowVAE (LOC)	87.0 (5.1)	75.2 (11.1)	28.3 (11.5)	47.7 (8.5)	86.9 (2.8)	4.4 (2.0)
SlowVAE (LAP)	100.0 (0.0)	97.5 (3.0)	29.5 (9.3)	65.4 (3.6)	96.5 (1.6)	8.1 (3.0)

Table 13: **dSprites.** Median and absolute deviation (a.d.) metric scores across 10 random seeds (first three rows are from (Locatello et al., 2020)). Bottom two rows give mean and standard deviation (s.d.) for the models presented in this paper.

Model (Data)	BetaVAE	FactorVAE	MIG	DCI	Modularity	SAP
β-VAE (*i.i.d.*)	100.0	87.9	8.8	22.5	90.2	1.0
Ada-ML-VAE (LOC)	100.0	87.4	14.7	45.6	94.6	2.8
Ada-GVAE (LOC)	100.0	90.2	15.0	54.0	93.9	9.4
SlowVAE (LOC)	100.0 (0.0)	90.4 (0.4)	15.7 (1.5)	48.9 (1.7)	95.7 (1.0)	1.6 (0.4)
SlowVAE (LAP)	100.0 (0.0)	91.0 (2.5)	9.7 (1.1)	51.0 (2.2)	94.4 (1.1)	1.7 (0.9)
SlowVAE (LOC)	100.0 (0.0)	90.4 (0.5)	15.4 (2.2)	48.0 (2.4)	95.4 (1.5)	1.6 (0.5)
SlowVAE (LAP)	100.0 (0.0)	90.2 (3.5)	10.4 (1.8)	50.9 (2.7)	94.1 (1.2)	2.0 (1.1)

Table 14: **Cars3D.** Median and absolute deviation (a.d.) metric scores across 10 random seeds (first three rows are from (Locatello et al., 2020)). Bottom two rows give mean and standard deviation (s.d.) for the models presented in this paper.

H.3 Latent Space Visualizations

We visualize differences in learned latent representations using image embedding in Figures 11- 24. We show four different plots for each dataset considered and include all available models. Each figure corresponds to a different dataset.

In Figures 11- 17 we display the mean correlation coefficient matrix and the latent representations for each ground-truth, as described in the main text for Fig. 4.

The top row is the sorted absolute correlation coefficient matrix between the latents (rows) and the ground truth generating factors (columns). The latent dimensions are permuted such that the sum on the diagonal is maximal. This is achieved by an optimal, non-greedy matching process for each ground truth factor with its corresponding latent, as described in appendix D. As such, a more prevalent diagonal structure corresponds to a better mapping between the ground-truth factors and latent encoding.

The middle set of plots are latent embeddings of random training data samples. The y-axis denotes the ground truth generating factor and the x-axis denotes the corresponding latent factor as matched according to the main diagonal of the correlation matrix. For each dataset, we further color-code the latents by a categorical variable as denoted in each figure.

The bottom set of plots show the ground truth encoding compared to the second best latent as opposed to the diagonally matched latent. This plot can be used to judge how much the correspondence between latents is one-to-one or rather one-to-many.

To further investigate the latent representations, we show a scatter plot over the best and second best latents in figures 18-24. Here, the color-coding is matched by the ground truth factor denoted in each row.

When comparing the correlation matrix with the corresponding scatter plots, one can see that embeddings with sinusoidal curves have low correlation, which illustrates a shortcoming of the metric. Another limitation is that categorical variables which have no natural ordering have an

Model (Data)	BetaVAE	FactorVAE	MIG	DCI	Modularity	SAP
β-VAE (*i.i.d.*)	74.0	49.5	21.4	28.0	89.5	9.8
Ada-ML-VAE (LOC)	91.0	72.1	31.1	34.1	86.1	15.3
Ada-GVAE (LOC)	87.9	55.5	25.6	33.8	78.8	10.6
SlowVAE (LOC)	85.4 (2.2)	54.7 (1.6)	24.9 (1.3)	31.8 (0.5)	86.5 (3.3)	6.3 (0.7)
SlowVAE (LAP)	87.4 (0.5)	74.0 (1.5)	27.8 (0.8)	42.4 (0.6)	97.7 (0.7)	8.2 (1.1)
SlowVAE (LOC)	85.0 (2.9)	54.9 (2.0)	24.6 (1.7)	31.9 (0.6)	85.3 (4.1)	6.3 (0.8)
SlowVAE (LAP)	87.1 (0.7)	73.4 (1.7)	28.1 (1.0)	42.4 (0.7)	97.3 (0.8)	7.5 (1.3)

Table 15: **SmallNORB.** Median and absolute deviation (a.d.) metric scores across 10 random seeds (first three rows are from (Locatello et al., 2020)). Bottom two rows give mean and standard deviation (s.d.) for the models presented in this paper.

Model (Data)	BetaVAE	FactorVAE	MIG	DCI	Modularity	SAP
β-VAE (*i.i.d.*)	98.6	83.9	22.0	58.8	93.8	6.2
Ada-ML-VAE (LOC)	100.0	100.0	50.9	94.0	98.8	12.7
Ada-GVAE (LOC)	100.0	100.0	56.2	94.6	97.5	15.3
SlowVAE (LOC)	100.0 (0.1)	97.3 (4.0)	64.4 (8.4)	82.6 (4.4)	95.5 (1.6)	5.8 (0.9)
SlowVAE (LAP)	100.0 (0.0)	95.9 (2.6)	62.5 (3.1)	85.6 (4.0)	98.1 (0.6)	8.2 (1.7)
SlowVAE (LOC)	99.9 (0.3)	95.4 (5.2)	58.8 (13.0)	82.3 (5.4)	95.2 (2.0)	5.7 (1.4)
SlowVAE (LAP)	100.0 (0.0)	95.0 (3.2)	61.5 (4.5)	85.0 (4.7)	98.3 (0.8)	8.9 (2.6)

Table 16: **Shapes3D.** Median and absolute deviation (a.d.) metric scores across 10 random seeds (first three rows are from (Locatello et al., 2020)). Bottom two rows give mean and standard deviation (s.d.) for the models presented in this paper.

order-dependent MCC score, indicating the permutation variance of MCC. With SlowVAE, we can infer three different types of embeddings. First, we have simple ordered ground truth factors with non-circular boundary conditions. Here, SlowVAE models often show a clear one-to-one correspondence (e.g. Fig 18 scale, x-position and y-position; Fig 21 θ-rotation; Fig 22 Φ-rotation). Second, we observe circular embeddings due to boundary conditions for certain factors (e.g. Fig 11, 18 3rd row; Fig 12, 19 2nd row). Note that not all datasets with orientations exhibit full rotations and thus do not have circular boundary conditions, e.g. smallNORB. Finally, we have categorical variables, where no order exists (e.g. Fig. 12, 19 top row, Fig 13, 20 top row, Fig 14, 21 top row) resulting in separated but not necessarily ordered clusters.

Model (Data)	BetaVAE	FactorVAE	MIG	DCI	Modularity	SAP
β-VAE (*i.i.d.*)	54.6	32.2	7.2	19.5	87.4	3.7
Ada-ML-VAE (LOC)	72.6	47.6	24.1	28.5	87.5	7.4
Ada-GVAE (LOC)	78.9	62.1	28.4	40.1	91.6	21.5
SlowVAE (LOC)	70.9 (3.5)	47.2 (2.8)	37.4 (8.0)	35.2 (1.3)	88.9 (1.0)	10.7 (1.2)
SlowVAE (LAP)	87.2 (2.9)	67.3 (6.2)	26.1 (2.9)	44.4 (2.1)	91.1 (1.4)	21.3 (2.1)
SlowVAE (LOC)	71.6 (4.4)	48.7 (3.7)	29.7 (9.8)	34.6 (1.7)	88.4 (1.3)	10.9 (1.5)
SlowVAE (LAP)	86.5 (3.5)	65.5 (8.3)	26.9 (3.1)	44.9 (2.6)	91.2 (1.7)	19.9 (4.7)

Table 17: **MPI3D.** Median and absolute deviation (a.d.) metric scores across 10 random seeds (first three rows are from (Locatello et al., 2020)). Bottom two rows give mean and standard deviation (s.d.) for the models presented in this paper.

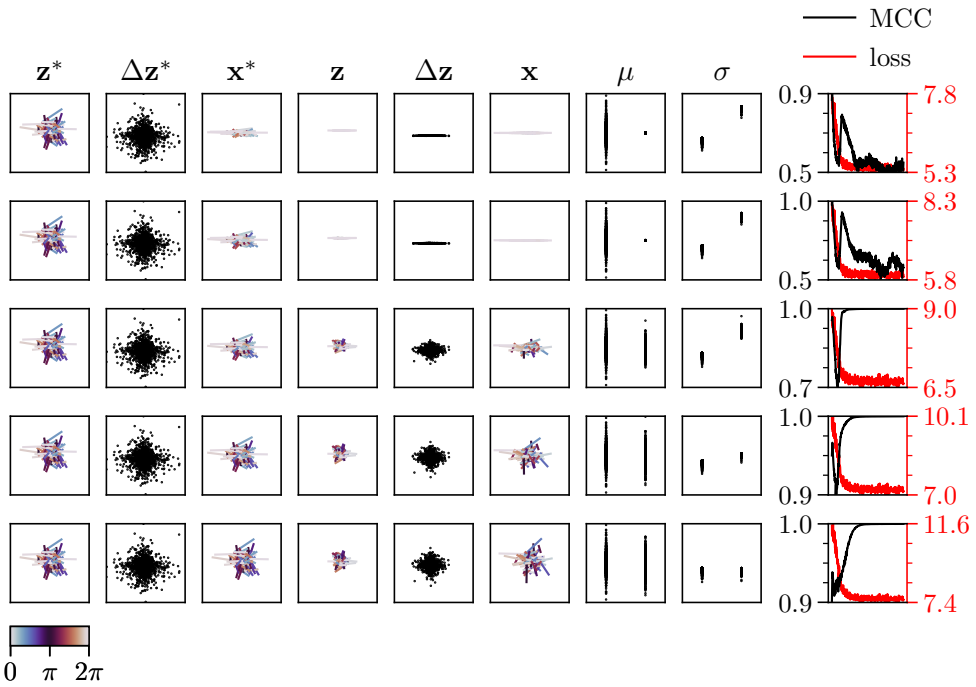

(a) SlowVAE performance.

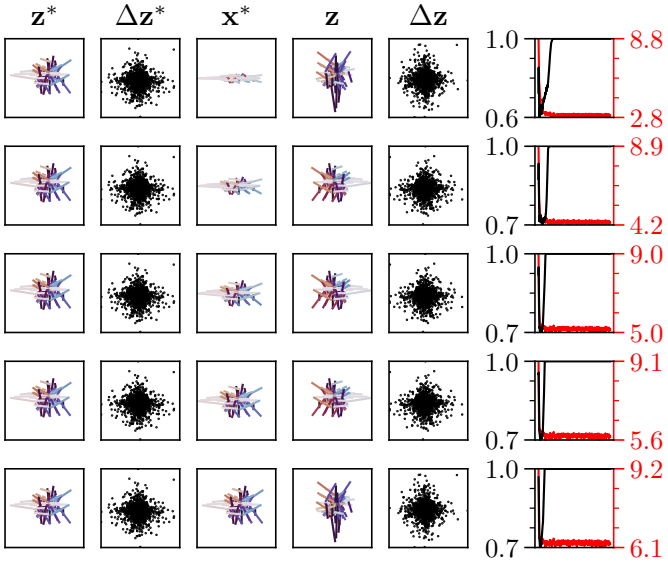

(b) SlowFlow performance.

Figure 6: **VAE failure modes.** Rows respectively indicate $\kappa = 0.2, 0.4, 0.6, 0.8, 1.0$ from equation (24). The left five columns show values for 100 randomly chosen examples, while the μ and σ columns show values for the full training set. Columns in the sets ($\mathbf{z}^*$, $\mathbf{z}$), ($\Delta\mathbf{z}^*$, $\Delta\mathbf{z}$), ($\mathbf{x}^*$, $\mathbf{x}$) all have the same (arbitrary) scale factors the axes. Lines indicate trajectories from time-point t to $t+1$, and color indicates the angle of the trajectory vector with respect to the canonical variable axes. The μ axes is scaled from -4 to 4, and σ axes are scaled from 0 to 1, where individual dots represent latent encoding values from test images. The rightmost plots show a shift in the relationship between the mean correlation coefficient (MCC) (black, higher is better) and training loss (red, lower is better) as one increases κ.

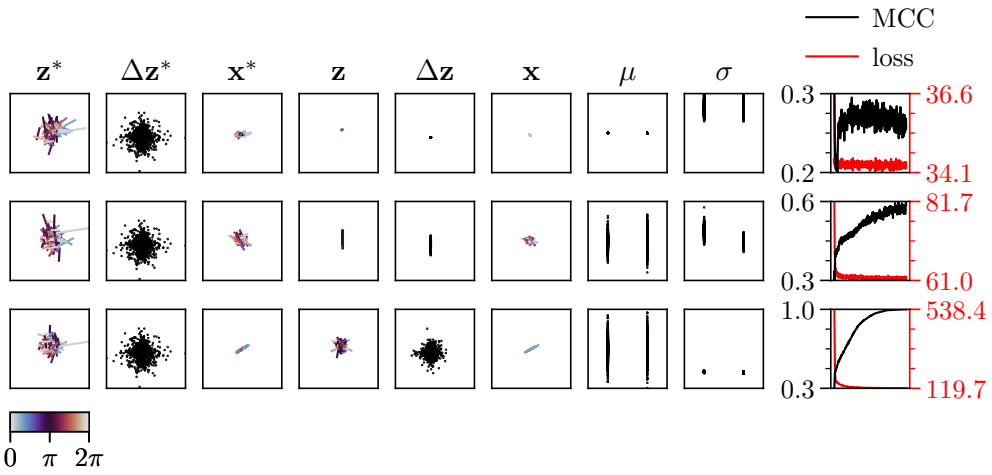

Figure 7: **VAEs perform better when data dimensionality exceeds the latent dimensionality.** VAEs prefer data dimensions to be greater than latent dimensions. Individual subplots are as described in Fig. 6. For all data in this experiment we used a 20-dimensional latent space, $\dim(\mathbf{z}^*) = 20$. Each row corresponds to the dimensionality of the $\mathbf{x}^*$, with values of 20, 200, and 2000. The first two dimensions of $\mathbf{z}^*$ are plotted as well as the two dimensions of $\mathbf{z}$ with the highest corresponding mean correlation coefficient (MCC). The $\mathbf{x}^*$ and $\mathbf{x}$ data are projected onto their first two principal component axes before plotting. A two-layer mixing matrix was used to transform data from Z_{gt} to X_{gt}. As one increases the data dimensionality, the SlowVAE network performs increasingly better in terms of MCC, although worse in terms of total training loss.

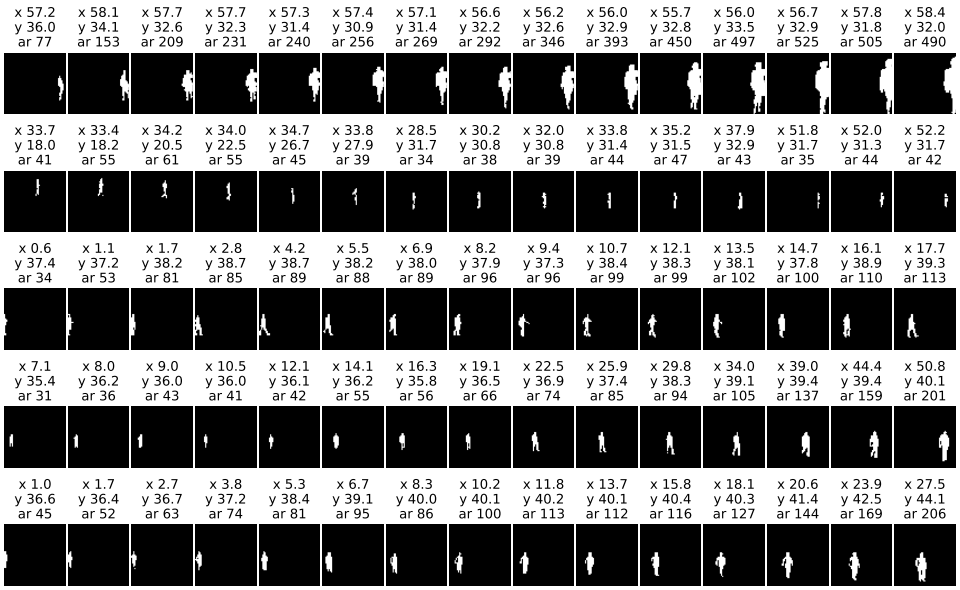

Figure 8: KITTI Masks : Each row corresponds to sequential frames from random sequences in the KITTI-Mssks dataset. Above each image we denote measured object properties where x, y correspond the center of mass position and ar corresponds to the area.

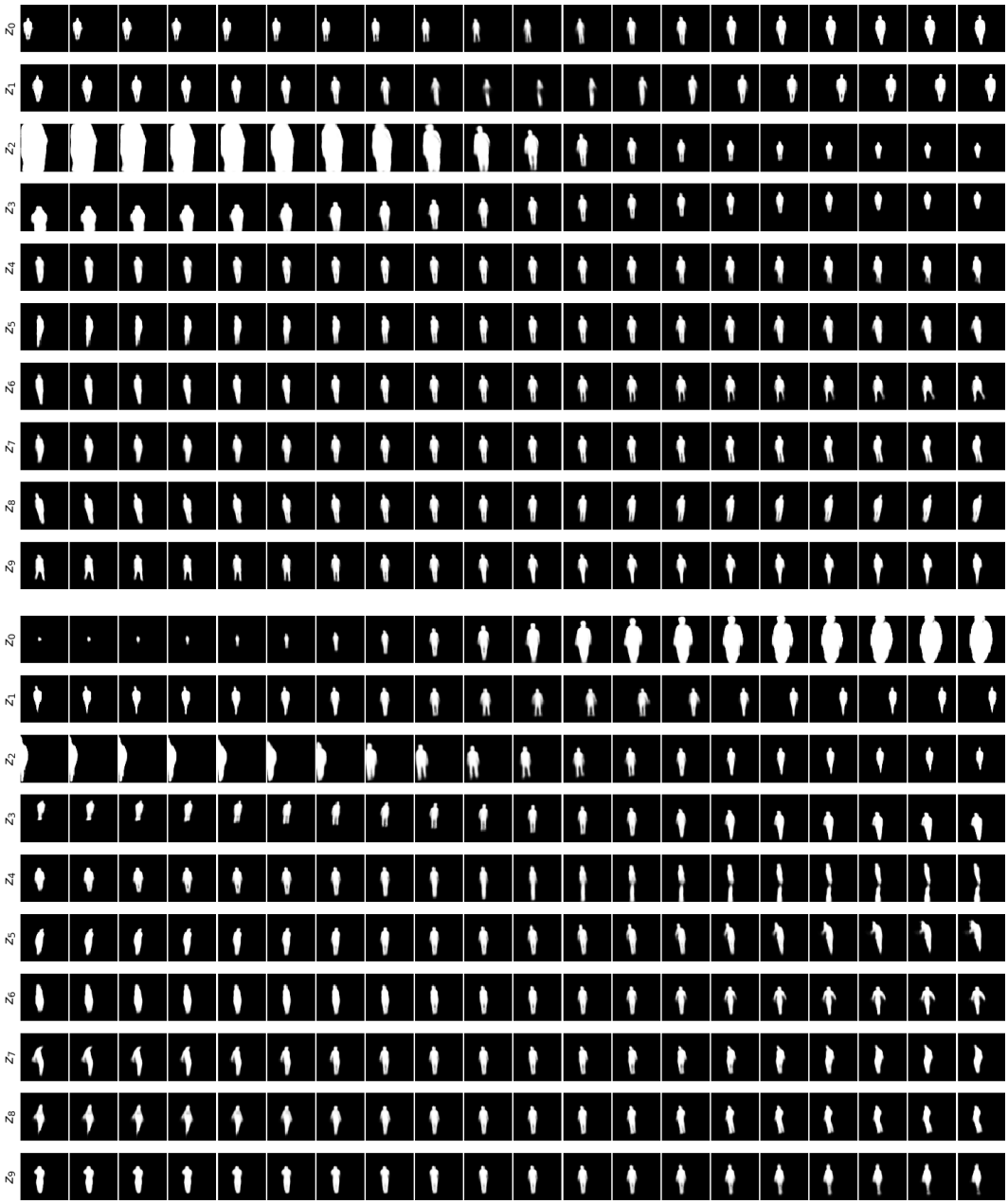

Figure 10: **KITTI Masks Latent Representations.** We show axis latent traversals along each dimension for the β-VAE (top) and SlowVAE (bottom). Here, the latents z_i are sorted from top to bottom in ascending order according to the mean variance output of the encoder. With MCC correlation (see e.g. Fig. 16) the known ground truth factors are matched as following: β-VAE: scale$\sim$ z_2, x-position$\sim$ z_1 and y-position$\sim$ z_3; SlowVAE: scale$\sim$ z_0, x-position$\sim$ z_1 and y-position$\sim$ z_3. With these latent visualizations alone, there is no significant difference visible between β-VAE and SlowVAE. However, we see a quantitative difference with the MCC score (see Table **??**) and a qualitative difference when directly observing latent embeddings (see Fig. 16).

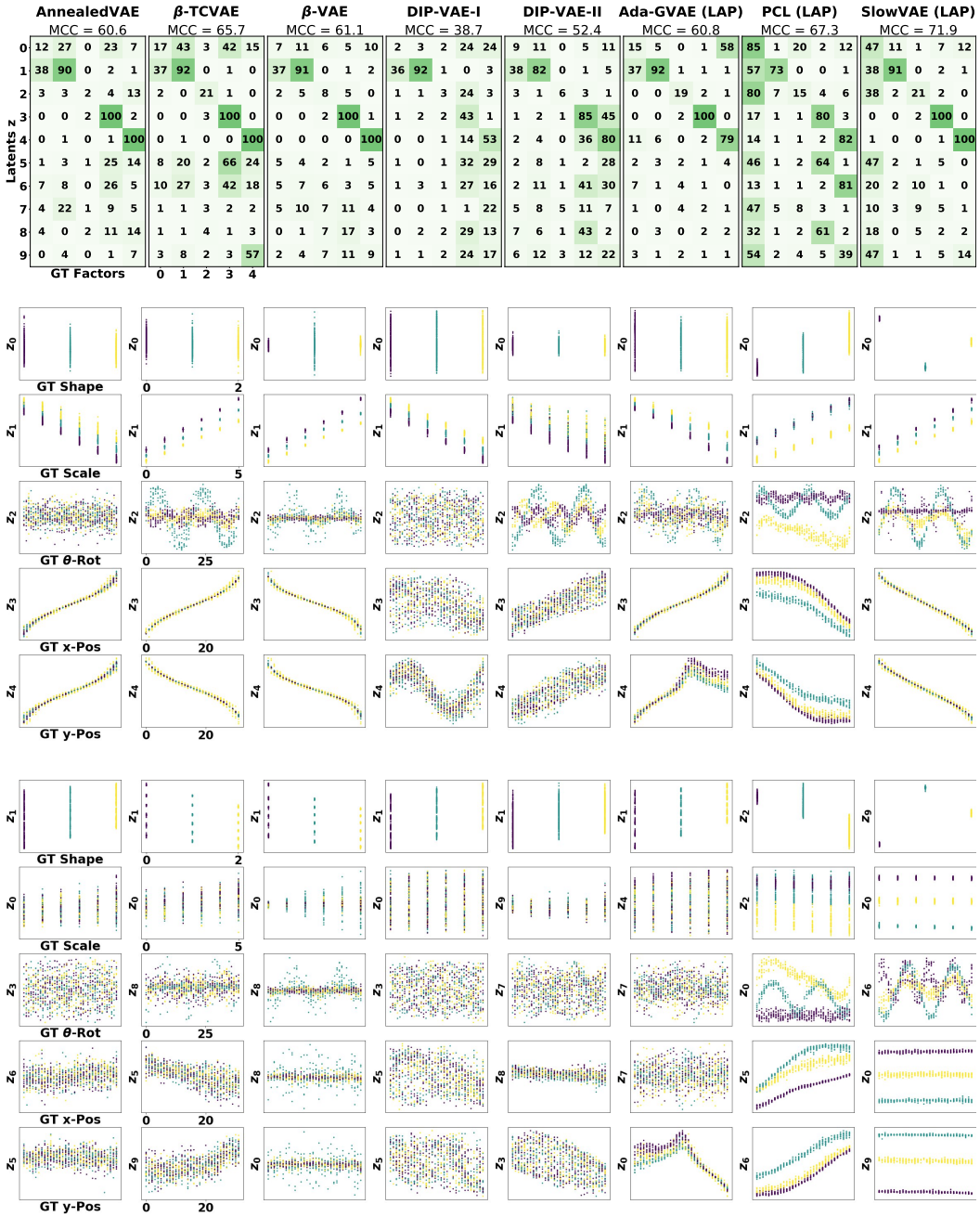

Figure 11: **DSprites Latent Representations.** Top, MCC correlation matrices. Middle five rows, model latent over highest correlating ground truth factor. Bottom five rows, model latent over second highest correlating ground truth factor. The color-coding corresponds to the shapes: heart/yellow, ellipse/turquoise and square/purple.

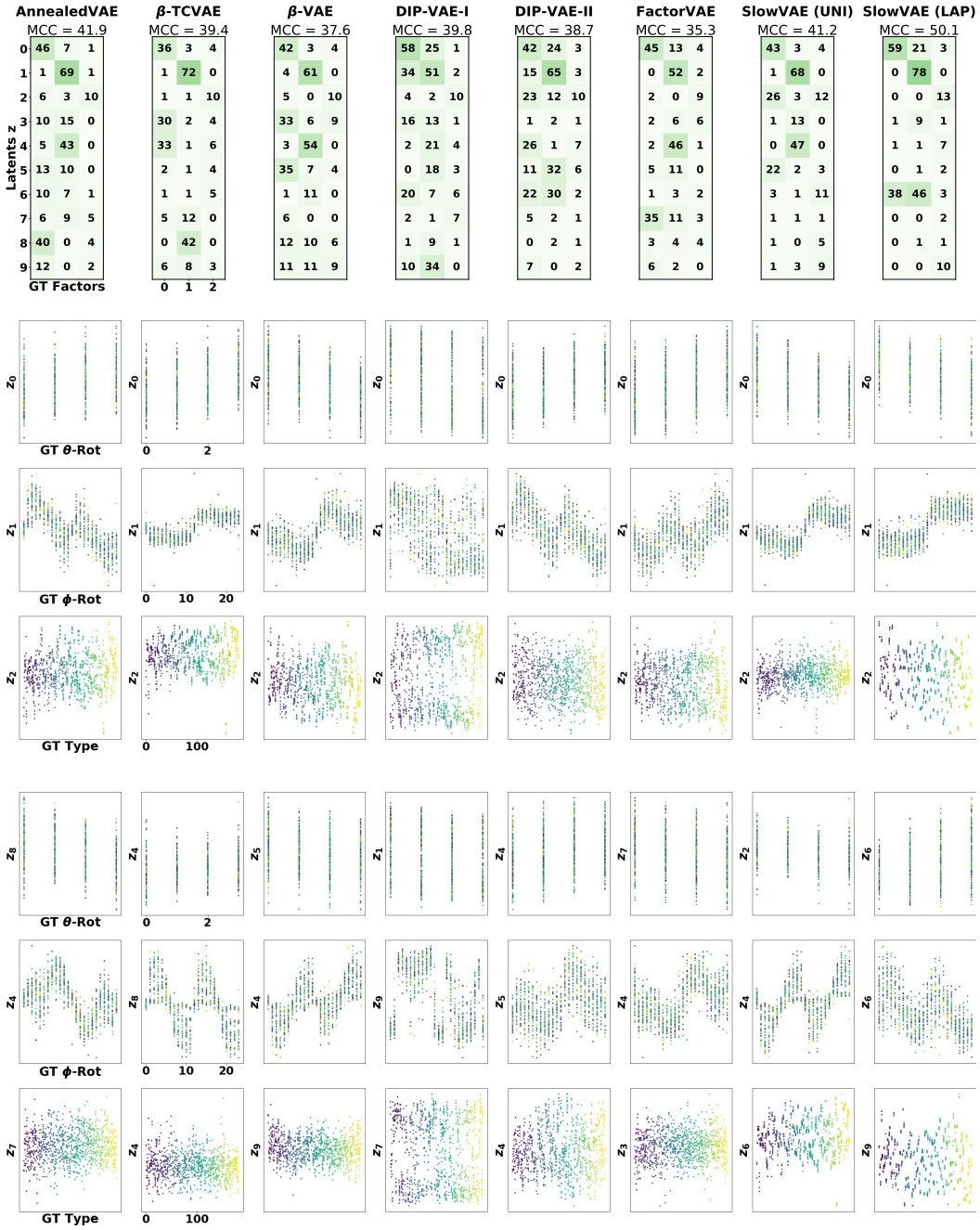

Figure 12: **Cars3D Latent Representations.** Top, MCC correlation matrices. Middle three rows, model latent over highest correlating ground truth factor. Bottom three rows, model latent over second highest correlating ground truth factor. The color-coding corresponds to the 183 different car types (GT Types) in the dataset.

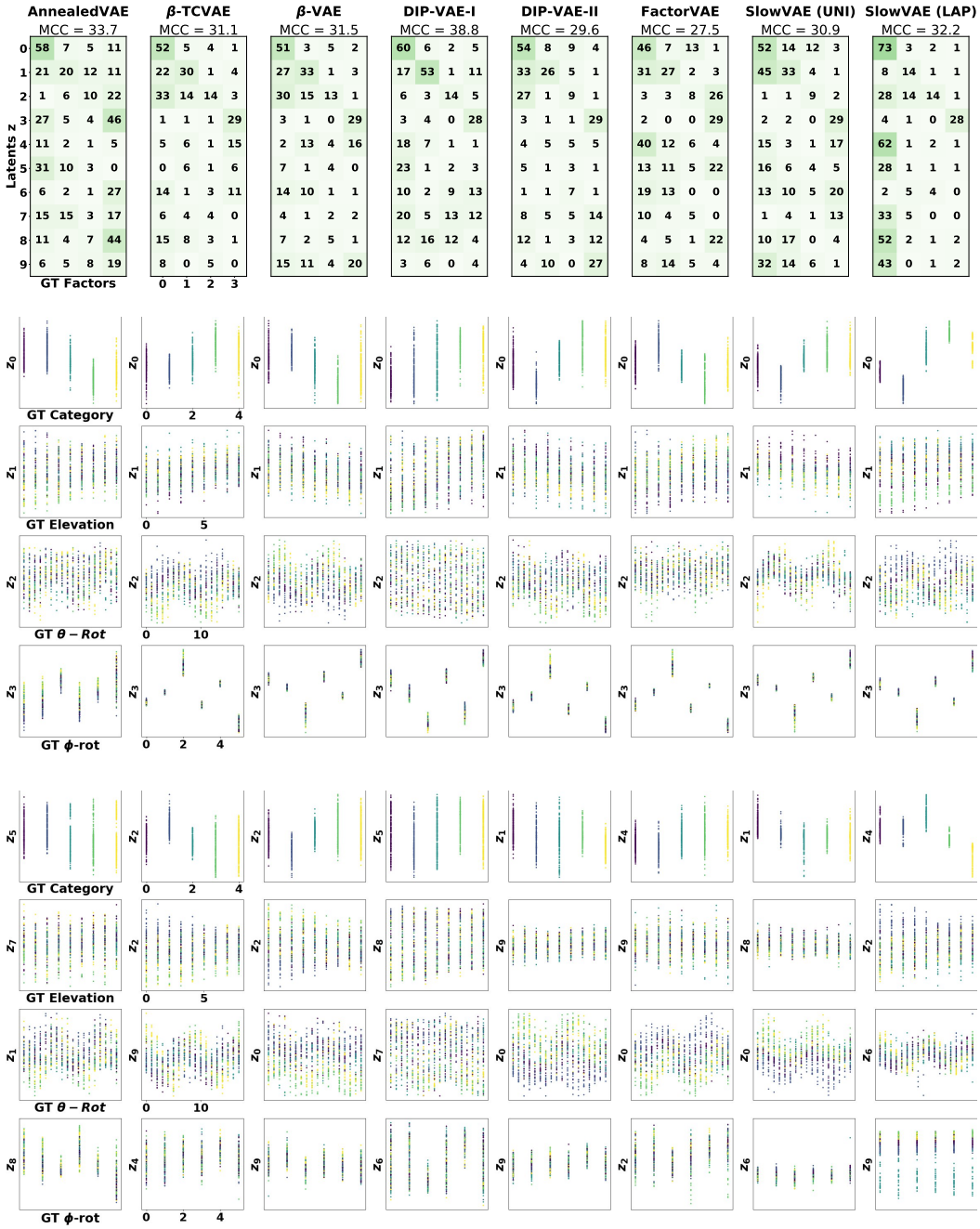

Figure 13: **SmallNorb Latent Representations.** Top, MCC correlation matrices. Middle four rows, model latent over highest correlating ground truth factor. Bottom four rows, model latent over second highest correlating ground truth factor. The color-coding corresponds to the five different GT categories in the dataset.

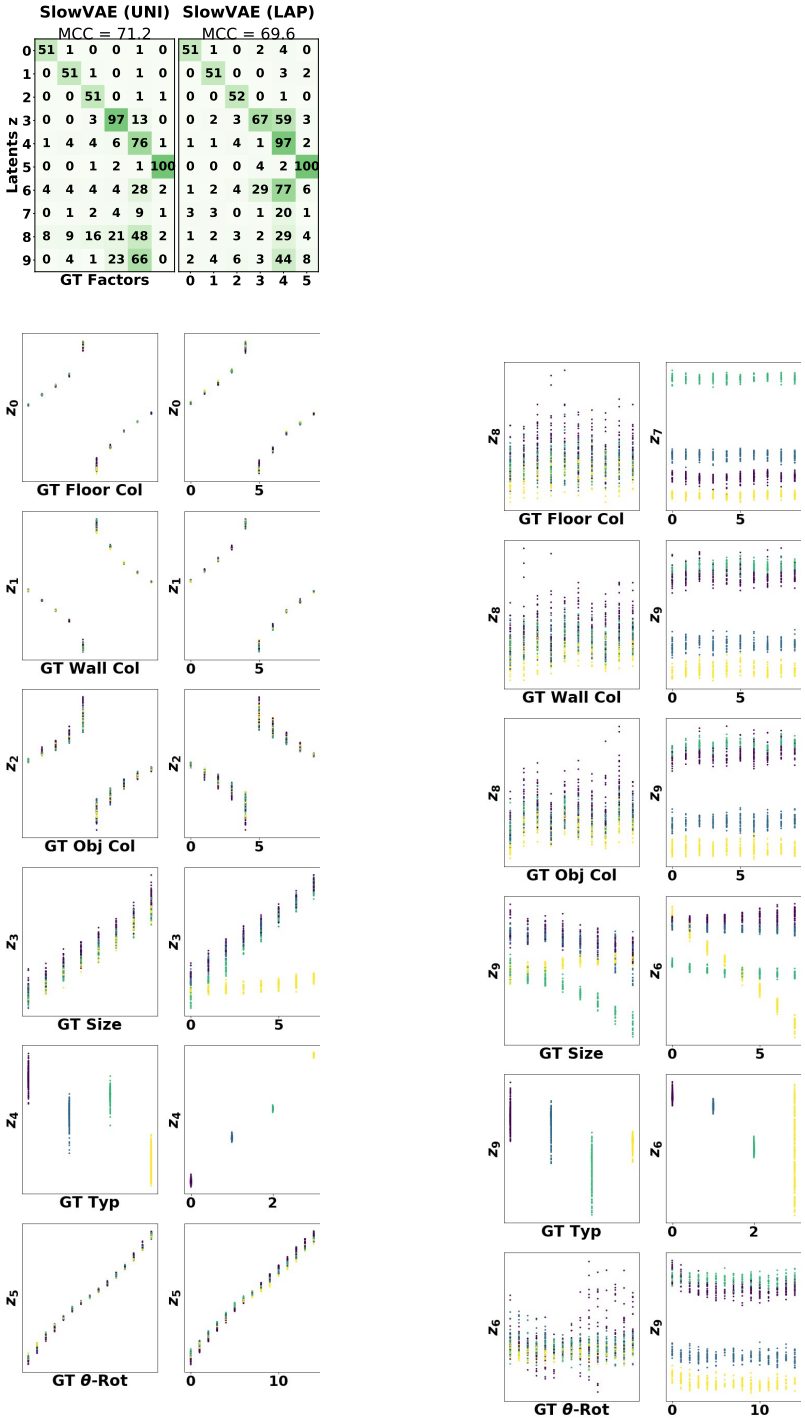

Figure 14: **Shapes3D Latent Representations.** Top, MCC correlation matrices. Left two columns, model latent over highest correlating ground truth factor. Right two columns, model latent over second highest correlating ground truth factor. The color-coding corresponds to the four different object types (GT-Type) in the dataset.

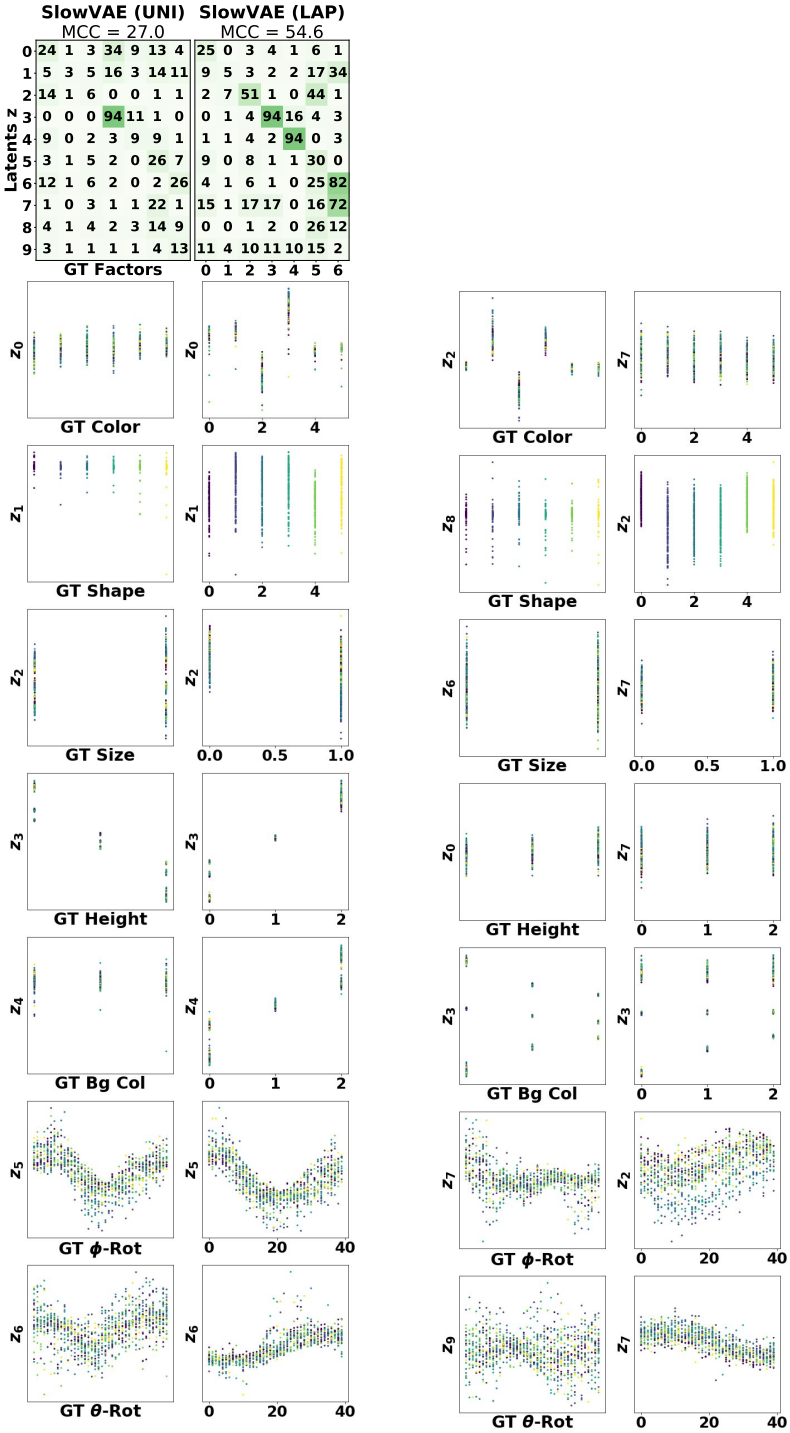

Figure 15: **MPI3DReal Latent Representations.** Top, MCC correlation matrices. Left two columns, model latent over highest correlating ground truth factor. Right two columns, model latent over second highest correlating ground truth factor. The color-coding corresponds to the six different object shapes (GT Shape) in the dataset.

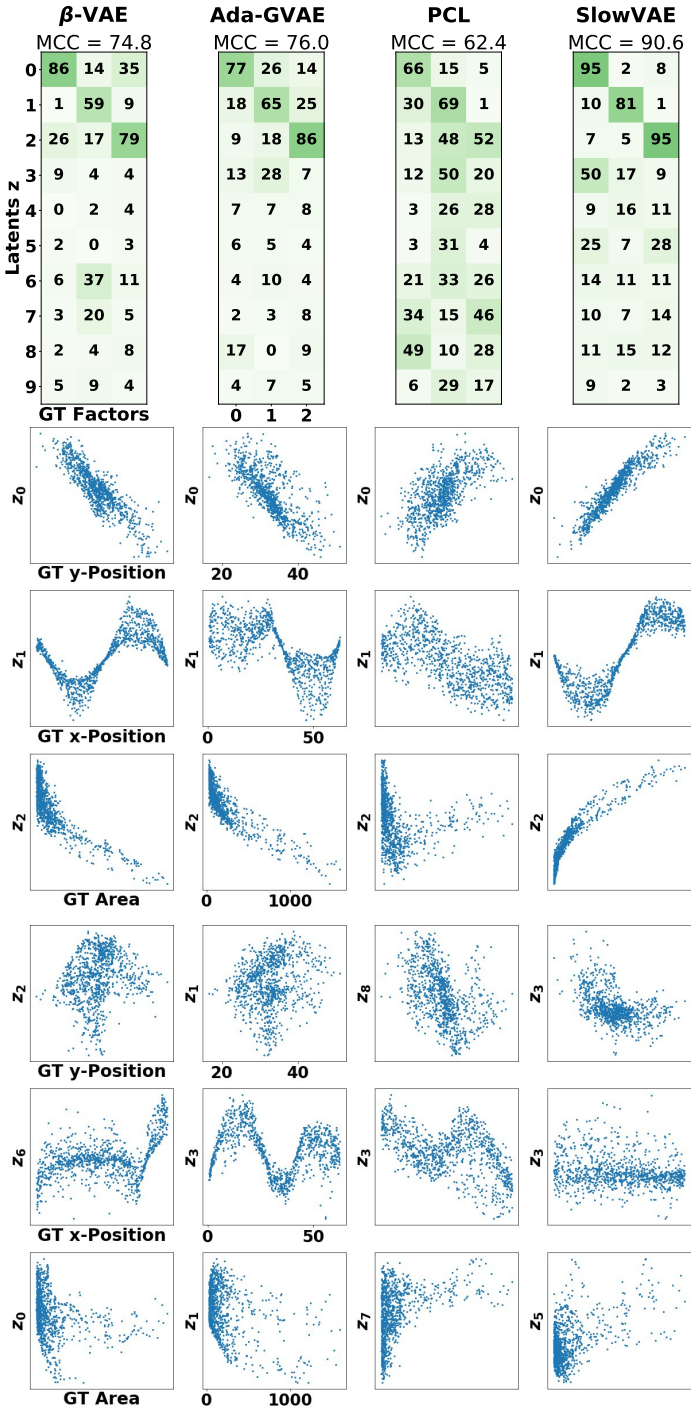

Figure 16: **KITTI Masks Latent Representations.** Top, MCC correlation matrices. Middle three rows, model latent over highest correlating ground truth factor. Bottom three rows, model latent over second highest correlating ground truth factor.

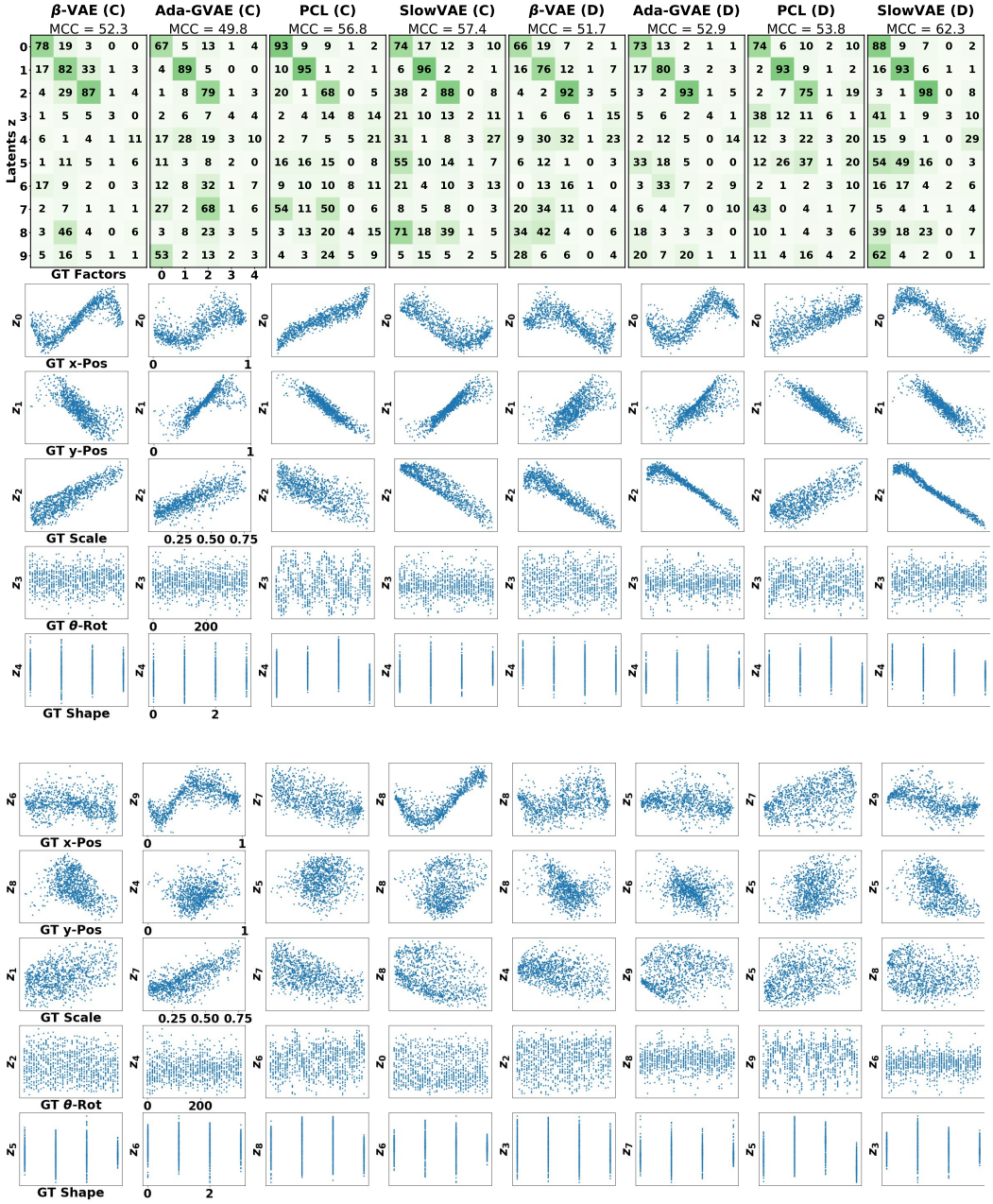

Figure 17: **Natural Sprites Latent Representations.** Top, MCC correlation matrices. Middle five rows, model latent over highest correlating ground truth factor (colored by category). Bottom five rows, model latent over second highest correlating ground truth factor. The left two columns denote the continuous (C) version of Natural Sprites, whereas the right two columns correspond to the discretized (D) version.

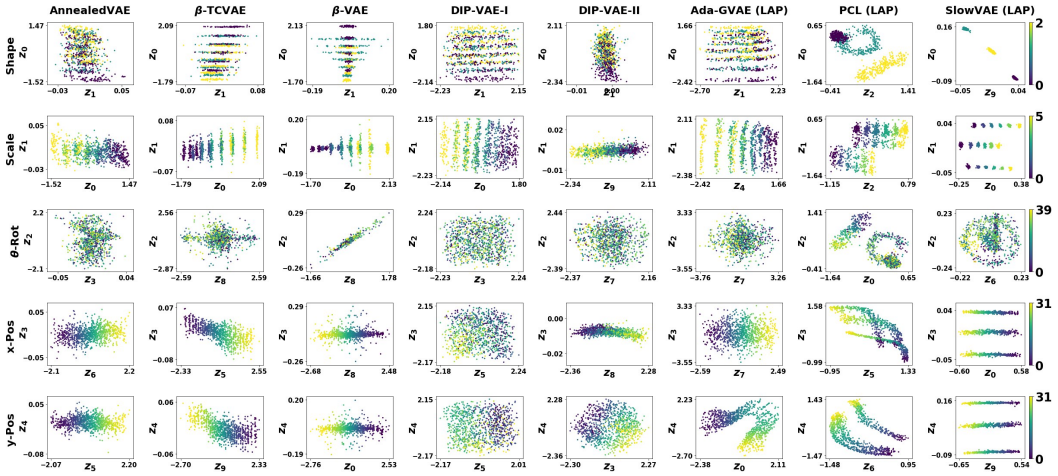

Figure 18: **DSprites Latent Representations**. Best two latents selected from Fig 11. Color-coded by the corresponding ground truth factor.

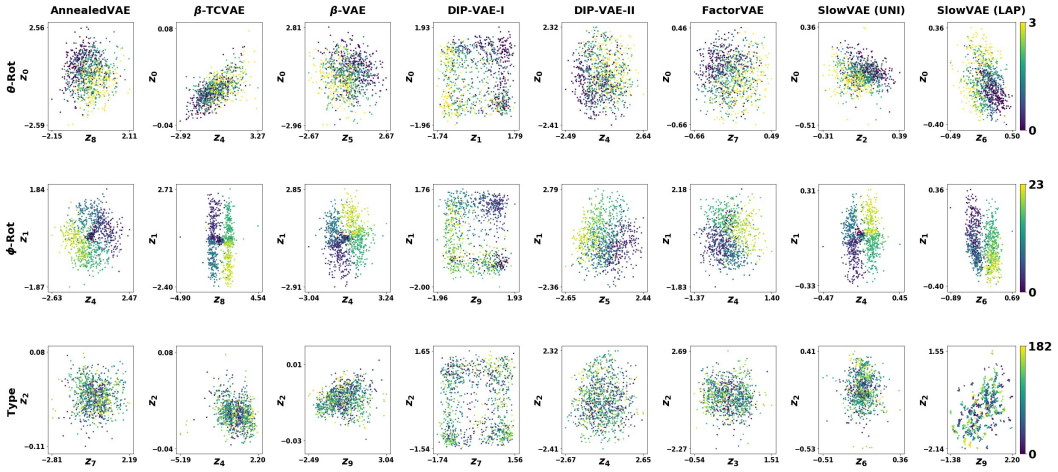

Figure 19: **Cars3D Latent Representations**. Best two latents selected from Fig 12. Color-coded by ground truth.

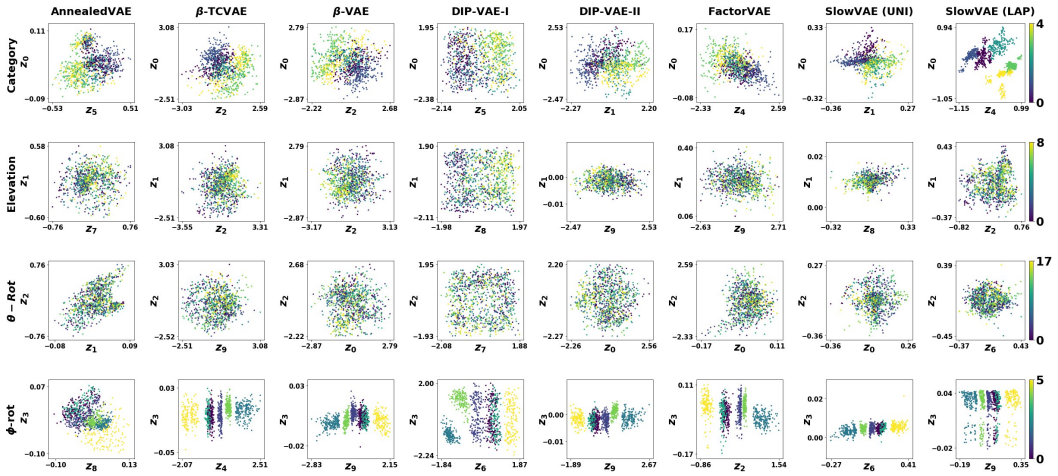

Figure 20: **SmallNorb Latent Representations**. Best two latents selected from Fig 13. Color-coded by ground truth.

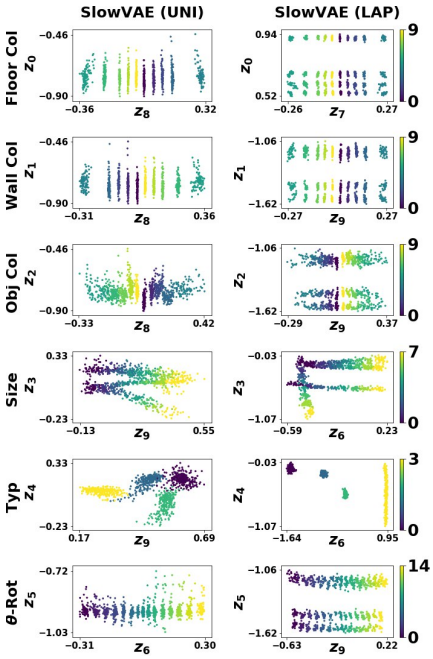

Figure 21: **Shapes3D Latent Representations**. Best two latents selected from Fig 14. Color-coded by ground truth.

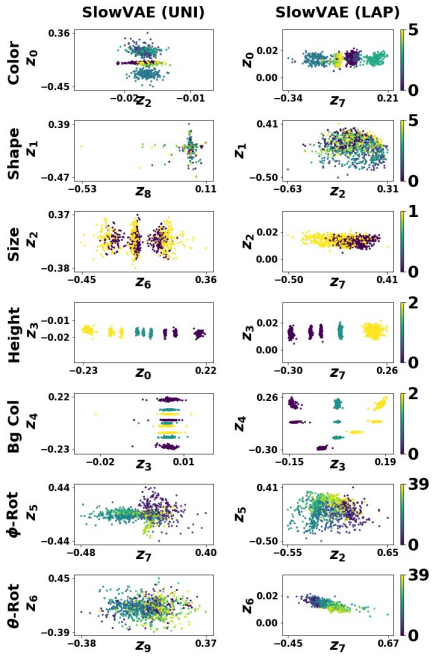

Figure 22: **MPI3DReal Latent Representations**. Best two latents selected from Fig 15. Color-coded by ground truth.

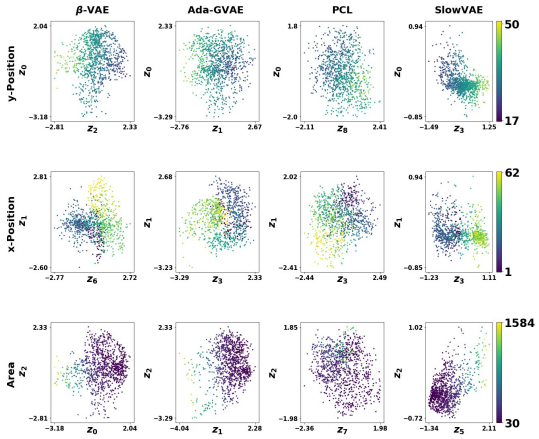

Figure 23: **KITTI Masks Latent Representations**. Best two latents selected from Fig 16. Color-coded by ground truth.

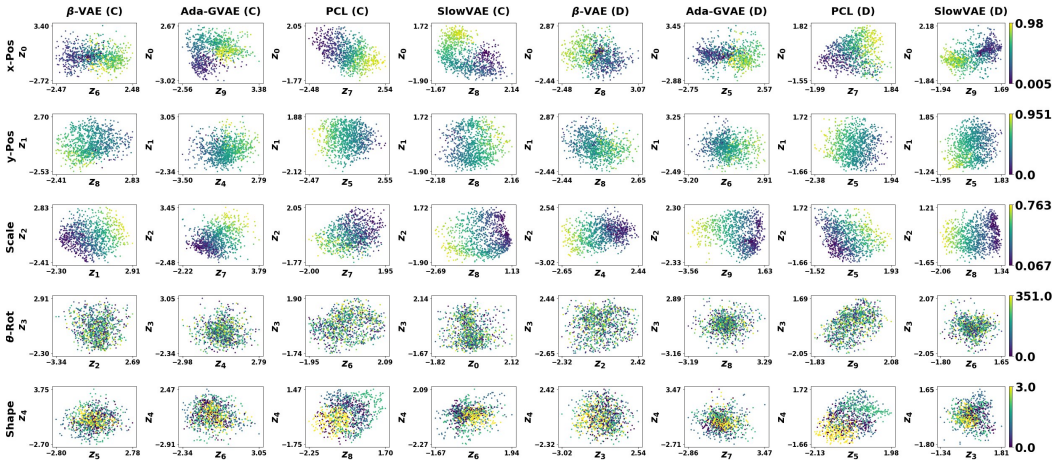

Figure 24: **Natural Sprites Masks Latent Representations**. Best two latents selected from Fig 17. The left two columns denote the continuous (C) version of Natural Sprites, whereas the right two columns correspond to the discretized (D) version. Color-coded by ground truth.